Studies on Visible Fluoride Fiber Lasers and White Light Emitting Fluoride Glasses

Hideyuki Okamoto

2014

Contents

General Introduction

Host glasses, such as those with fluoride, chloride, bromide, or iodide compositions, which generally have low phonon energies, have higher emission efficiencies due to the low non-radiative decay rates and high radiative emission rates of rare-earth ion levels [1, 2]. Since the discovery of fluorozirconate glass in 1975 [3], glass formation seems to have become more common in halide systems. In particular, the ZrF_4–BaF_2–LaF_3–AlF_3–NaF (ZBLAN) composition [4] has been considered the most stable and practical glass for optical fiber applications. For these reasons, fluoride glasses and fibers are excellent candidates for fiber lasers in the visible and mid infrared region where emissions are hard to be obtained from silicate and phosphate fibers.

Ultraviolet (UV)–visible lasers are used in various applications such as laser projection displays, optical data storage, photolithograpy, holograph, microscopy, laser processing, and biology. Until now, UV-visible lasers could be obtained in three general methods [5]: (1) using a non linear frequency doubling or tripling process, (2) through upconversion of rare-earth doped materials with low phonon energy, and (3) by using a short wavelength semiconductor laser such as GaN and ZnSe. When using nonlinear devices, the tight tolerances for the pump wavelength and the severe temperature control of nonlinear crystal are drawbacks for practical applications. By contrast, an upconversion laser was first demonstrated by L.F. Johnson et al., with Er^{3+}-Yb^{3+} and Ho^{3+}-Yb^{3+} codoped BaY_2F_8 crystals [6]. Since then, upconversion fiber lasers have been reported with various rare earth ions, such as Pr^{3+} [7], Nd^{3+} [8], Ho^{3+} [9], Er^{3+} [10] and Tm^{3+} [11] in the UV–visible wavelength.

Additionally, directly pumped visible fiber lasers, which excited from the ground state to the emission state, have also been demonstrated, for example, Pr^{3+}:ZBLAN fiber laser pumped

by an Ar ion laser [12] or an optically pumped semiconductor laser [13]. Although these pumping sources are voluminous for practical applications, high power GaN blue lasers have been commercially available as next generation pump sources [14]. The wavelengths of visible ZBLAN fiber lasers pumped with various pumping sources were summarized in Fig.1 [5, 15]. The applications of fluoride glass fiber lasers are not restricted to the UV–visible region only. Fluoride glasses have a weaker bonding strength compared to silica glasses, because the fluorine ion is singly charged, which means the transmission range of fluoride glasses in the infrared region is wider than that of silica glasses. Many infrared ZBLAN fiber laser, based on Nd^{3+} [16], Tm^{3+} [17], Ho^{3+} [18], Er^{3+} [19], and Dy^{3+} [20] have also been reported.

Fluoride glass fiber lasers are remarkable laser media with a wide range, from the UV to infrared region. However, they have some significant drawbacks in terms of mass production. One drawback is that the procedure to make fluoride glass and draw fibers is complicated. Fluoride fibers are known to occasionally have scattering due to various defects in the fiber [21]. Therefore, it is essential to discuss the defects in the fiber before investigating properties of the fiber laser. I first prepared the fluoride fiber from raw materials; the defects in the fiber are discussed in the thesis.

Then, I focused on the tunability of Pr^{3+} doped fluoride fiber. Although the emission spectrum of Pr^{3+} ions spreads continuously from the visible to near-infrared (NIR) wavelength [22], the oscillation band of Pr^{3+}:ZBLAN fiber laser were separated. I investigated this and expanded the range of turnability, which is described in the second chapter.

As mentioned above, there is no doubt that rare earth ion doped fluoride fibers are an excellent gain medium for UV–visible–NIR applications, however, ZBLAN fibers have low water durability compared with silicate fiber [23]. Nevertheless, most resonators on ZBLAN fiber lasers have dichroic mirrors attached to the end of the fiber, and a lens focuses the pump

light into the fiber core. Thus, the ends of the fluoride fiber are exposed to air. This may be a critical problem for practical use, and it is why fluoride fiber laser have not been commercially used. One method to prevent damage at the ends of fluoride fiber is to splice the fiber to a more stable silica fiber. Fiber pigtailed semiconductor lasers are also available, for example, a pump laser at 980 nm for an optical amplifier. Therefore, a pump laser can be directly spliced to fiber without air gap, which makes it easy to achieve an all fiber laser. In this case, using a fiber Bragg grating (FBG) is the simplest way to construct laser cavities, however, Ge-doped fiber used for a FBG was photo sensitive to short wavelength light [24]. Therefore I propose a new laser cavity structure consisting of a dielectric mirror at the splicing point, and demonstrated the laser operation in the green wavelength region.

Solid state forms of illuminations such as light emitting diodes (LEDs) have been attracting interest recently for their potential use as efficient light sources. Generally, white LEDs have conventionally been fabricated with yellow phosphor (YAG:Ce^{3+}) and blue GaN chips [25] . However, several problems with the light quality from these types of white LEDs have been reported, including poor color rendering, color shifts caused by changes in current, and an uncomfortable glare.

In the last chapter of this thesis, I investigate the applicability of rare earth fluoride glass for white LEDs. The laser operations mentioned above are based on 4f-4f transitions of rare-earth ions. The excitation and emission bands are narrow because the 4f orbital was shelled by outer orbitals. On the contrary, divalent ions such as Eu^{2+} [26] and Yb^{2+} [27] can stably exist in fluoride glasses, and they indicate broad band emission based on 5d-4f transitions. In particular, Yb^{2+} doped fluoride glass shows white emission under deep UV excitation [27]. While this glass phosphor has high quantum efficiency (QE), the excitation wavelength (deep-UV) is much shorter than visible wavelengths; thus, thermal losses corresponding to Stokes shifts are

unavoidable in visible applications. Consequently, in the final chapter I report the potential use of Yb^{2+}:fluoride glasses excited with near-UV light for visible applications.

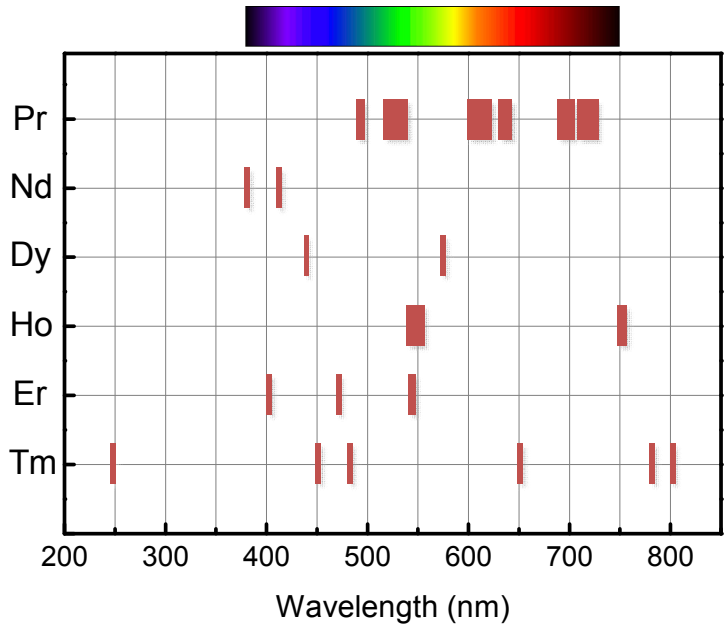

Fig.1. Wavelength of UV–infrared laser transitions in ZBLAN.

Summary of each chapter

Chapter 1: Fluoride glass fiber for visible laser was prepared. The process involved steps from melting raw materials to drawing the fluoride fiber. Preform was prepared by extrusion molding of core/cladding composite glass made by casting. A drawn fiber included some defects in its core, so we investigated the origin of the defects to suppress the loss of the fiber to be used for the fiber laser.

Chapter 2: A CW tunable PDF laser operation over a 300-nm range (479–497, 515–548, 597–737, and 849–960 nm) pumped by a single GaN LD from a single 9-cm PDF was prepared. The total tunable range is 6469 cm^{-1}, which was wider than that of conventional Ti:sapphire lasers. The revealed ultra-wide tunability of PDF lasers is useful for laser TVs, biomedical applications, and other uses. Lasers in the cyan–green region are significant for expanding the color reproduction range of laser TVs and laser projections.

Chapter 3: The new laser cavity structure for low melting fiber is proposed and a demonstration of it is described. I developed an all-fiber laser resonator by fusion splicing both sides of a PDF to end-coated silica fibers. The maximum output power and the slope efficiency of the 521-nm fiber laser were 322 mW and 53%, respectively. The slope efficiency is the highest value obtained for a green fiber laser. The characteristics of the dielectric mirror did not change after splicing; therefore, this technique of splicing two materials with different Ts values is practical for all-fiber lasers.

Chapter 4: We successfully prepared white luminescent Yb^{2+}:AlF_3-based fluoride glasses that were efficiently excited with near-UV light. Fluoride glasses containing Hf or Zr that melted under an H_2/Ar atmosphere exhibited bluish white luminescence, but the co-existence of Yb^{2+} and Hf^{3+}/Zr^{3+} resulted in the suppression of white luminescence. In contrast, the white luminescence of Yb^{2+} was notably intensified by incorporating chloride by replacing BaF_2 with $BaCl_2$ and $SrCl_2$. Although the highest reduction ratio ($\Delta = Yb^{2+}/(Yb^{2+} + Yb^{3+})$) was only 45% for the chloride-containing glass, η_{in} was 42% and η_{ex} was 34%. Further improvements in the QE are required for practical visible applications; such enhancements can be achieved by analyzing the mechanism responsible for chloride incorporation.

References

1. Y. Hatefi, N. Shahtahmasebi, A. Moghimi, and E. Attaran, Journal of Rare Earths **29**(5), 484 (2011).
2. K. Annapurna, R. N. Dwivedi, and S. Buddhudu, Materials Letters **53**, 359 (2002).
3. M. Poulain, M. Poulain, and J. Lucas, Materials Research Bulletin **10**(4), 243 (1975).
4. K. Ohsawa, T. Shibata, K. Nakamura, and S. Yoshida, in Proceedings of the 7th European Conference on Optical Communication (ECOC), pp. 1.1-1–1.1-4, Copenhagen, Danmark, September 1981.
5. X. Zhu, and N. Peyghambarian, Advances in OptoElectronics, 2010 (2010).
6. L. F. Johnson and H. J. Guggenheim, Applied Physics Letters **19**(2), 44 (1971).
7. R. G. Smart, D. C. Hanna, A. C. Tropper, S. T. Davey, S. F. Carter, and D. Szebesta, Electronics Letters **27**(14), 1307 (1991).
8. D. S. Funk, J. W. Carlson, and J. G. Eden, Electronics Letters **30** (22), 1859 (1994).
9. D. S. Funk and J. G. Eden, IEEE Journal of Quantum Electronics, **37**(8), 980 (2001).
10. J. Y. Allain, M. Monerie, and H. Poignant, Electronics Letters **28**(2), 111 (1992).
11. R. M. El-Agmy, Laser Physics **18**(6) 803 (2008).
12. R. G. Smart, J. N. Carter, A. C. Tropper, D. C. Hanna, S. T. Davey, S. F. Carter, and D. Szebesta, Optics Communications **86**, 333 (1991).
13. A. Richter, H. Scheife, E. Heumann, G. Huber, W. Seelert, and A. Diening, Electronics Letters **41**, 794 (2005).
14. Y. Fujimoto, J. Nakanishi, T. Yamada, O. Ishii, and M. Yamazaki, Progress in Quantum Electronics **37**, 185 (2013).

15. M. J. F. Digonnet, Rare-Earth-Doped Fiber Lasers and Amplifiers, 2nd edn., CRC Press, Boca Raton, FL (2001).

16. T. Komukai, Y. Fukasaku, T. Sugawa, and Y. Miyajima, Electronics Letters **29**(9), 755 (1993).

17. M. Eichhorn and S. D. Jackson, Applied Physics B **90**(1), 35 (2008).

18. J. Schneider, C. Carbonnier, and U. B. Unrau, Applied Optics **36**(33), 8595 (1997).

19. H. Toebben, Electronics Letters, 28(14), 1361 (1992).

20. S. D. Jackson, Applied Physics Letters, 83(7), 1316 (2003).

21. J. S. Sanghera and I. D. Aggarwal, J. Am. Ceram. Soc., 76(9), 2341 (1993).

22. H. Okamoto, K. Kasuga, I. Hara, Y. Kubota, Electron. Lett., **44**(23), 1346 (2008).

23. C. J. Simmons, and J. H. Simmons, Journal of the American Ceramic Society, 69(9), 661 (1986).

24. K. Médjahdi, F. Goutaland, A. Boukenter, and Y. Ouerdane, Journal of Non-Crystalline Solids, 351, 1835 (2005).

25. K. Bando, K. Sakano, Y. Noguchi, and Y. Shimizu, Journal of Light and Visual Environment 22, 2 (1998).

26. J. Qiu, K. Miura, N. Sugimoto, and K. Hirao, Journal of non-crystalline solids, 213, 266 (1997).

27. J. W. M. Verwey and G. Blasse, J. Phys. Chem Solids **53**, 1152 (1992).

Chapter 1

Preparation of fluoride glass and fluoride glass fiber

1.1 introduction

Fluoride glass fiber has been developed many years to achieve the low loss fibers for long-hole telecommunications at infrared band, because their minimum theoretical loss is about 0.001 dB/km [1]. Fluoride glass is well known as low phonon energy glass, therefore the glasses shows low non-radiative decay and high radiative emission rates of rare earth ion energy level [2]. Rare earth doped fluoride fiber lasers are reported from UV to infrared region [3-6], therefore fluoride fiber is promising material for UV–infrared applications.

However, obtaining high quality long fluoride fiber is more difficult than obtaining silicate fiber. In practice, the loss of fluoride fiber is usually more than 1–10 dB/km, because of scattering from defects which include bubbles, submicrometer platiunm particles, oxyfluorides, and fluoride microcrystals [7].

Until now, many type of fluoride glass compositions have been investigated, especially fluorozirconate glasses commonly called ZBLAN which is the most stable among all heavy metals fluoride compositions [8, 9]. Recently fluoroalminate glass has been also demonstrated [10], however, the thermophysical properties of the glass are higher than those of flurozirconate glass [11] and they may decrease the stability of fiber drawing. Therefore, the ZBLAN glass was chosen as a host glass for visible fiber laser.

In this chapter, I prepared fluoride fiber from melting raw material to draw fiber and evaluated the defects in the fiber.

1.2 Preparation of preform

There are various methods of forming fluoride glass fiber preforms, such as rod-in-tube method [12], cladding-over-casting [13], build-in casting [13,14], and rotational casting [15], and suction casting [16]. In the case of these methods, some of drawbacks were mentioned [17]: for example, bubbles and striae tend to be incorporated into the glass, generation of irregular interface between the core and the cladding. In order to suppress these defects, we casted core melt on a flat horizontal upper surface of cladding melt as mentioned in Section 1.2.4. We first melted the two mixtures for core and cladding glasses. The procedure is discussed in the following section.

1.2.1 Melting fluoride glasses and preparation of core/cladding composite glass

The composition of core and cladding were determined in advance to match thermo-physical properties of each glass as listed in Table 1. The glass transition temperature (T_g) and the crystallization temperature (T_x) were measured with Rigaku DSC8270 differential scanning calorimeter. The cladding refractive index was controlled by the amount of HfF_4 which decreases refractive index [18]. All fluoride raw materials were high purity grade (Fe, Ni, Co, Cu < 50 ppb, O < 100 ppm) and obtained from Central Glass Co., Ltd. The weights of batches were 50g for core and 120g for cladding, which were determined by considering the heat flow during the casting process. After mixing the raw materials, NH_4FHF (1% by weight) was added to fluoride mixture to eliminate the residual oxide impurities. The batches were set into the glassy carbon crucibles (external diameter 40 mm, internal diameter 35mm, height 50

mm). The entire procedure, from mixing the raw materials to cooling the melt, was carried out in an N_2-filled glove box directly equipped with an atmosphere controllable furnace.

Table 1 Core and cladding glass composition for preparing preform

	ZrF_4	HfF_4	BaF_2	LaF_3	AlF_3	YF_3	NaF	ReF_3	T_g	T_x
Core	53		22	2.5-x	3.5	2	17	x	274	349
Cladding	10	40	19	3	4	2	22		274	389

Compositions and temperatures (x=0) are in mole percentages and degrees Celsius.

1.2.2 Melting atmosphere for fluoride glasses

Fluoride glasses are commonly melted under reactive atmosphere (RAP: Reactive atmosphere process), such as CCl_4 [19], SF_6 [20], CS_2 [21], NF_3 [22], for several purpose. In this thesis, I used Cl_2 gas as a reactive atmosphere for convenience. The dry inert atmosphere, which is necessary to ensure melts free of OH^-, is frequently able to reduce the melt. In case of the fluorozirconate melts, a reduced form Zr^{3+} occurs black deposites in glasses [23], however, oxidizing atmosphere enable obtain transparent glass.

Another purpose of using RAP is to reduce both OH^- and O^{2-} contamination [24]. Cl_2 can be used according to

$$O^{2-}_{(m)} + Cl_{2(g)} \rightarrow 2Cl^-_{(m)} + 1/2O_{2(g)} \quad (1\text{-}1)$$

$$2OH^-_{(m)} + Cl_{2(g)} \rightarrow 2Cl^-_{(m)} + H_2O_{(g)} + 1/2O_{2(g)} \quad (1\text{-}2)$$

The reactive gas has a strong oxidizability and also helps to suppress reduced zirconium species.

1.2.3 Heating mixtures and casting melts

The heating profile of fluoride mixtures was shown in Fig.2. At first, the mixtures were set into the glassy carbon crucibles and heated to 350 °C and kept for 1 h to eliminate oxide impurities. In the case of zirconium, the chemical reactions using ammonium bifluoride occurrs to eliminate oxide impurities as follows [25]:

$$2ZrO_2 + 7NH_4FHF \rightarrow 2(NH_4)_3ZrF_7 + 4H_2O + NH_3 \quad (1\text{-}3)$$

$$(NH_4)_3ZrF_7 \xrightarrow{-NH_4F} (NH_4)_2ZrF_6 \xrightarrow{-NH_4F} NH_4ZrF_5 \xrightarrow{-NH_4F} ZrF_4 \quad (1\text{-}4)$$

The other oxide impurities in the other raw material were eliminated same way.

After that, Cl_2 gas was additionally started flowing into the furnace and the partial pressure of Cl_2 was 0.5%. The furnace was heated up to 875°C with 30 min and kept for 60 min.

Next, the crucible of cladding melt was taken out from furnace at 650 °C temporarily, then a holey glassy carbon disk, which have 5 mm diameter of center hole, was set on the surface of cladding melt. After that, the crucible was promptly returned into the furnace and then heated up to 875 °C for 60 min again. After that, two melts were kept at 650°C for 1h to homogenize their temperature.

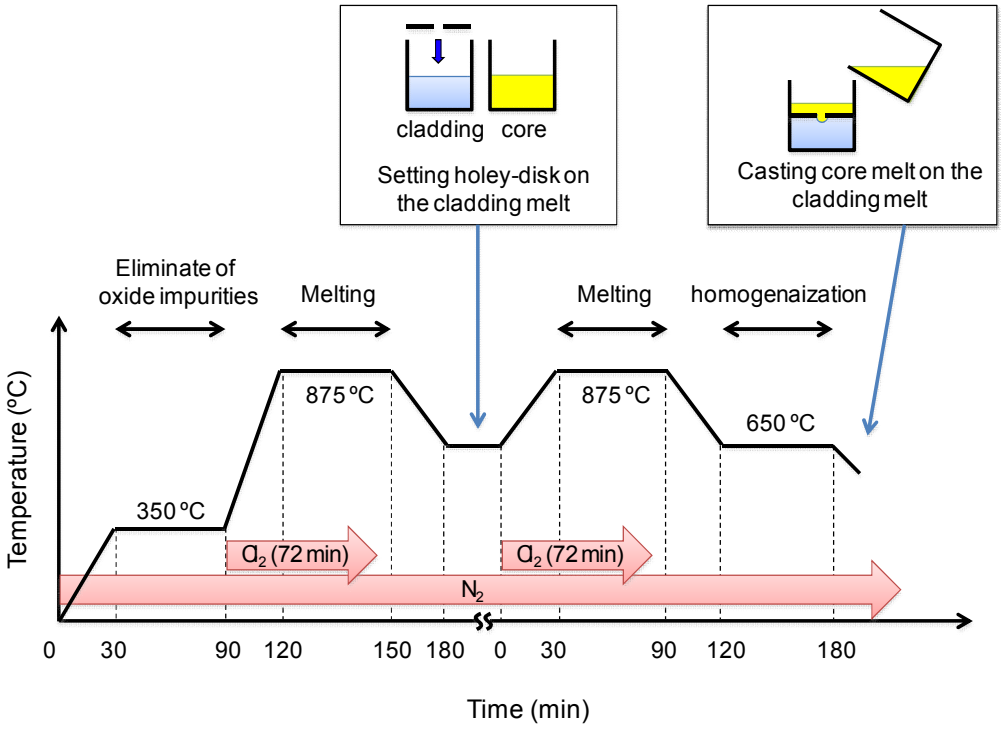

Fig.2. Heating profile for core and cladding glass

1.2.4 Casting core melt on cladding melt

On the final phase of melting, the core melt was cast on the cladding melt using the following procedure. In order to control the cooling speed of the melts, the cladding melt was taken out from the furnace and was put on a glassy carbon pedestal which had been heated to 275°C (Fig.3(a)). As the melt cooled down, the volume of the cladding melt decreased and the surface of the cladding melt stated sinking (Fig.3(b)). 5 min after, the core melt was also taken out from the furnace and was cast on the glassy carbon disk (Fig.3.(c)). The core started intruding into the cladding melt until the shrinkage of the cladding melt stopped.

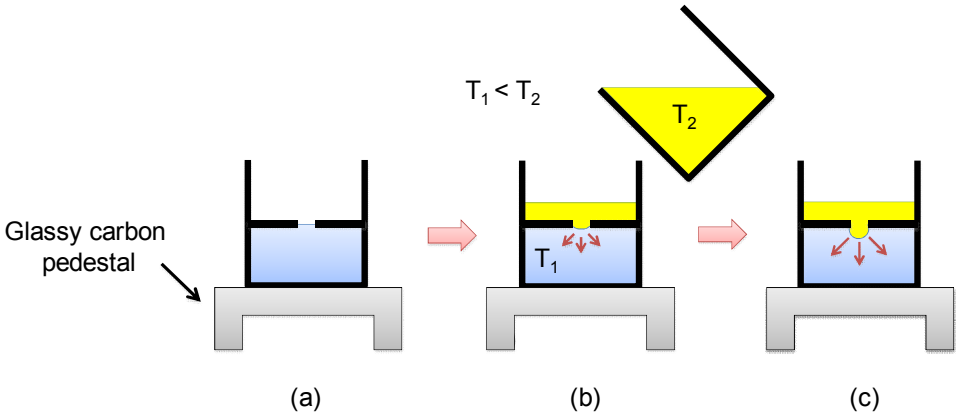

Fig.3. Casting core glass melt on the cladding glass with glassy carbon disk which have 5.0 mm diameter center hole.

1.2.5 Extrusion molding for fiber preform

Fig.4 shows the core-cladding composite bulk glass (35 mm diameter) prepared in the previous section. The top surface of the composite glass was polished to a certain radius (D_{bulk}) of core glass as shown in Fig.4(a). The D_{bulk} would correspond to a diameter of the fiber core. The bottom surface of the glass was also polished to obtain 20 mm thickness of composite glass.

The concept of preparation methods for fiber preform using extrusion molding were proposed by Kawamoto et al. and Miura et al. [25, 26]. Fig.5 shows the schematic diagram of the extrusion molding used in this experiment. The extrusion molder was directly equipped to N_2 filled glove box and all the procedure of extrusion molding was made under an inert gas. The whole inner parts of extruder, which contact to fluoride glass directly, were made by SUS 304 stainless steel. The polished core-cladding composite glass was set in the die which has 6 mm diameter of hole in the bottom. The glass was then heated by furnace up to 330°C, which is higher than softening temperature of ZBLAN glass. Here, the temperature of the glass was measured at the bottom surface by contacting a thermocouple directly until an extrusion was started. Once the glass reached the temperature, the glass was pushed by the punch with the pressure of 4.5 MPa. Few hours later, the approximately 6 mm diameter of preform was obtained as shown in Fig.6.

The obtained preform had core and cladding structure, however, the diameter of the core in the preform was not constant. Fig.7 shows the distribution of diameters of core and cladding of the preform measured using Mitsutoyo QV404 3D CNC Vision Measuring System. During the measurement, the preform was immersed into the matching oil (n_d=1.47) which has a little higher refractive index than the cladding glass. It enabled to detect both boundaries optically between core/cladding and cladding/matching-oil. The preform would be drawn to fiber in the

following section while keeping fiber diameter 125 μm. The core diameter of the fiber, calculated using the raito of core/cladding diameter of preform, is also shown in Fig.7. The relationship between D_{bulk} of composite glass and a diameter of fiber core is shown in Fig.8. These two parameters were well-correlated with each other, therefore, the core diameter of fiber can be controlled by D_{bulk}. In this thesis, the desired core of 3.5~4.0 μm was attained when the composite glass was polishes to 4.5~5.0 mm of D_{bulk}.

Finally, we measured refractive indices of core and cladding glass with Karunyu KPR-200 refractometer as shown in Fig.9. The measured points were fitted by Sellmeier equation,

$$n = \sqrt{1 + \sum_i \frac{B_i \lambda^2}{\lambda^2 - C_i}} \tag{1-5}$$

Where n is the refractive index, λ is the wavelength in vacuum, and B_i and C_i are experimentally determined Sellmeier coefficients.

The numerical aperture (NA) of a fiber is determined by core and cladding indices as:

$$NA = \left(n_1^2 - n_2^2\right)^{1/2} \tag{1-6}$$

Where n_1 and n_2 are refractive indices core and cladding, respectively. The result shows that, on the whole visible to near infrared wavelength (400–750 nm), NA of prepared fiber was approximately 0.22 .

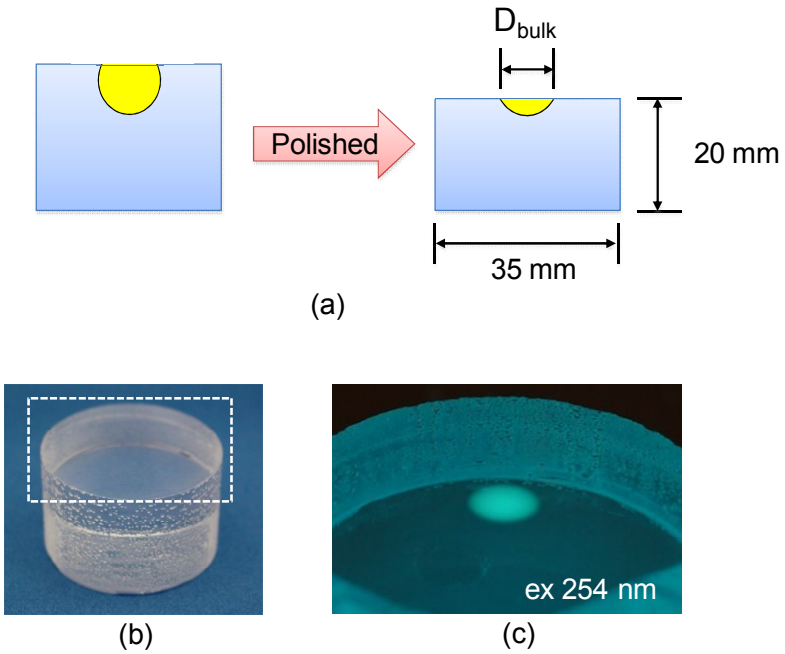

Fig. 4. Core-cladding composite glass obtained by casting. (a) Top surface was polished to obtain desired core glass radius D_{bulk}. (b) Photograph of polished glass and (c) Top surface of polished glass exited at 254 nm UV light. Core glass was doped with 3000 ppm of Er^{3+}.

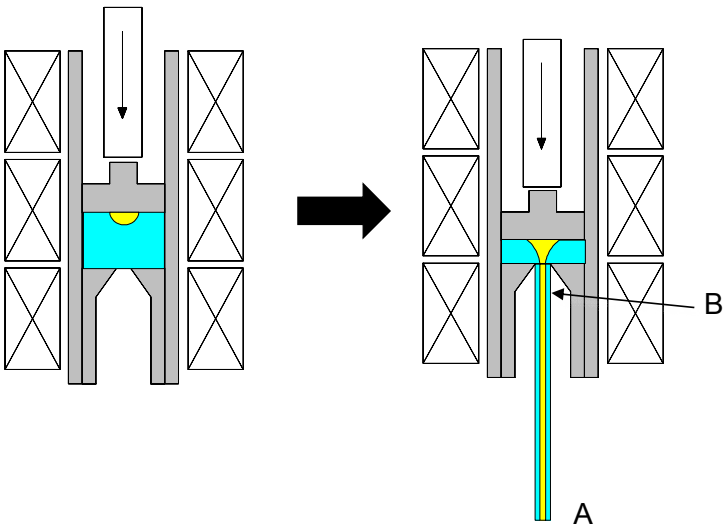

Fig. 5. Extrusion molding of fluoride fiber preform.

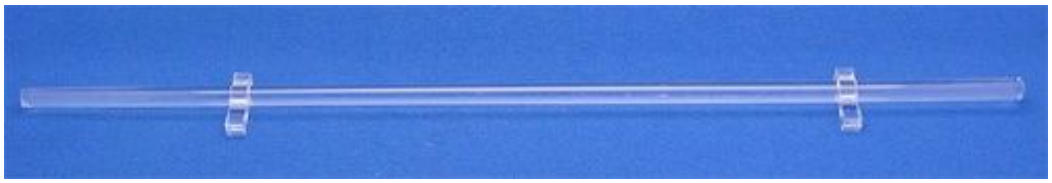

Fig. 6. Obtained fiber preform by extrusion method.

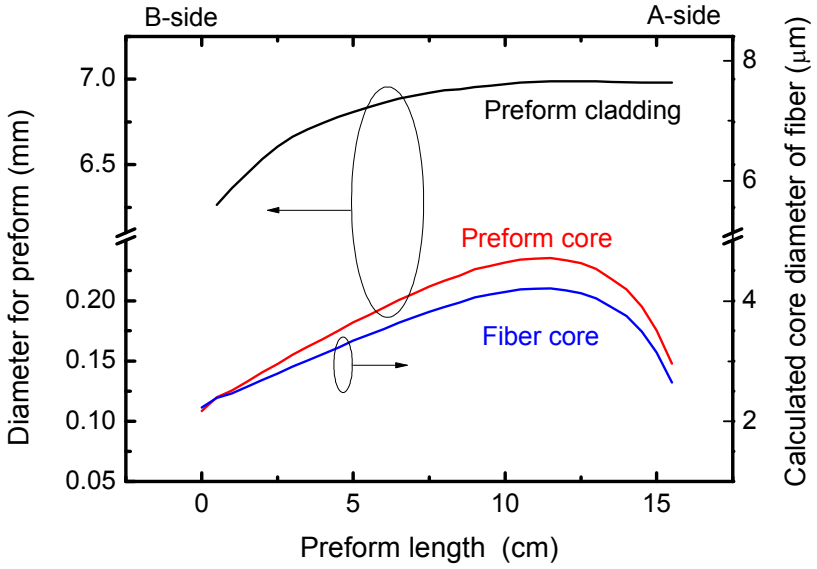

Fig. 7. Distribution of diameters of core and cladding for preform (left Y axis). The preform would to be drawn and stretched to fiber which has 125 μm of cladding diameter in the next section. The corresponding core diameter of the drawn fiber which is calculated with the cladding / core ratio of the preform is also shown in right Y axis.

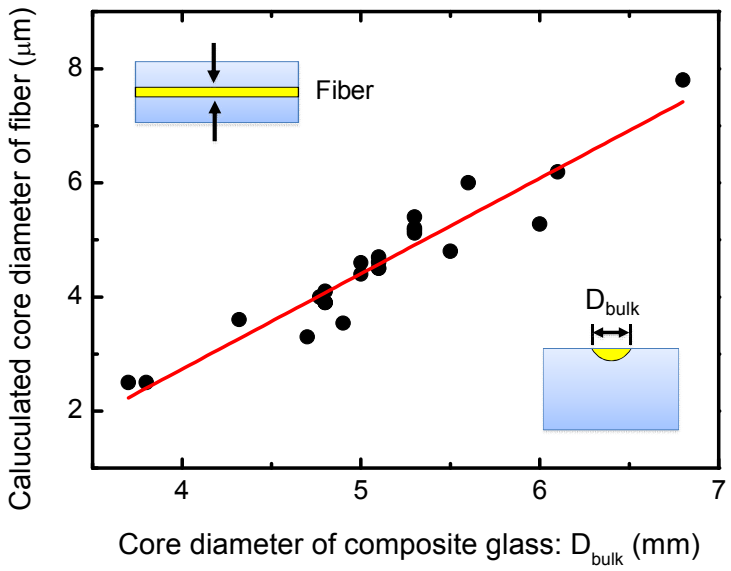

Fig. 8. Relationship between the diameter of composite glass core (Dbulk) and the diameter of the core fiber.

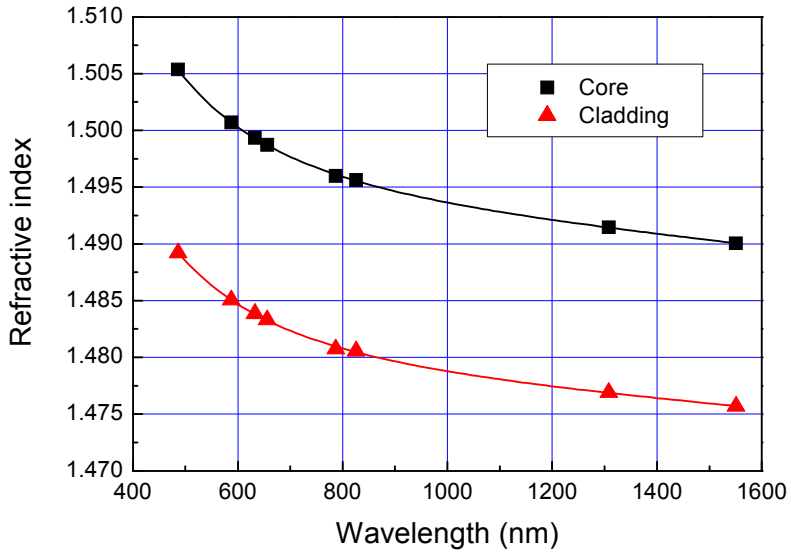

Fig. 9. Refractive indices of core and cladding glasses.

1.3 Drawing fluoride fiber

It is well known that the strength of a fluoride fiber greatly depends on the condition of the surface of preform [27]. Before fiber drawing, the preform was etched by mixed solution of 1wt% $ZrCl_2O \cdot 8H_2O$ in 1N HCl for 10 min. The etching rate of cladding glass was 1.2 μm/min. After the etching, the preform was shortly rinsed in HCl and then H_2O. After that, the H_2O was wiped out completely with wiping cloth (Kim towel white, Nippon Paper CRECIA Co., Ltd.), then evaporated residual H_2O on the surface of the preform at 320°C in vacuum.

After that, ZBLAN fiber was drawn by the fiber drawing tower described in Fig.10. The prefrom was fixed to stainless steel rod, which was gripped by the feeder. A 25g weight was attached at the bottom edge of the preform, then the middle part of preform was heated to 330°C by furnace which had 4 cm of soaking area. Once the furnace reached the desired temperature, the preform was partially softened and drew, then the bottom part of preform dropped. After that, the thread in between separated preform was pulled by a capstan roller which was controlled to maintain fiber diameter to 125μm. While drawing fiber, the preform feeder was used to lower the preform into the furnace at 2.2 mm/min.

The drawn fiber was coated by UV curable resin, Desolite KZ8758 (JSR, Japan) and cured by UV-lamp which have 254 mm length and 80 W/cm of output power. The obtained diameter of UV-coated fiber was 250 μm.

Note that the entire process from heating preform to curing the UV curable resin were processed under N_2 atmosphere to prevent the reaction of the surface of preform.

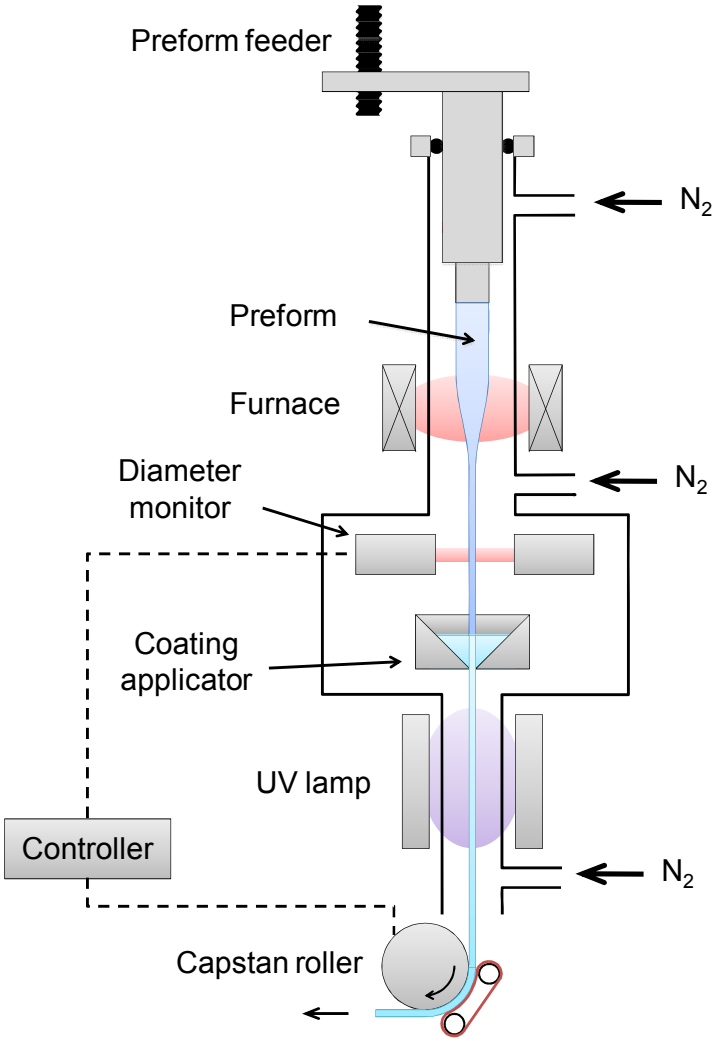

Fig. 10. Fiber drawing tower

1.4 Evaluation of prepared fluoride fiber

In the first phase of evaluations, UV-coating of the edge of fiber was swollen by acetone for few minutes then stripped off. After that, the bared fiber was cleaved using YORK FK-11 fiber cleaver. A core and a cladding diameter of fiber were measured using EXFO NR-9200 optical fiber analyzer. The distribution of measured core diameter was consistent with the calculated value shown in Fig.7.

The transmission loss of the fiber was measured with a halogen lamp and an ADVANTEST Q8383 optical spectrum analyzer (OSA) as shown in Fig.11. The inset shows experimental setups of the cut-back method. As a result, the transmission loss of the 5-m-length of fiber at 635 nm was 0.35 dB/m.

In order to observe and investigate the defects in fiber core, 635-nm semiconductor laser was coupled into the core of the fiber, then some bright spots were visualized as shown in Fig.12(a). The cross sections of defects were exposed by cleaving and etching then observed using Hitachi S3000N scanning electron microscope (SEM) and optical microscope. These defects were: Pt particle, bubbles and crystallization in the core. The first type of the defect was sub-micrometer particle as shown in Fig.12(b), and was identified Platinum (Pt) by analyzing using EDAX DX-4 Energy Dispersive X-ray Spectroscopy as shown in the inset. Pt particle might be from ZrF_4 raw material. Due to the fact that the vapor pressure of ZrF_4 is approximately 100 times higher greater than that of transition metal fluorides, the sublimation will give a good separation. The sublimation was made using Pt boat [28]. Therefore, this Pt is considered to be the origin of the Pt contamination. Fig.12 (c) shows the cross section of the second type of defect: the bubbles distorted core shape. The bubbles observed were not located on the boundary between core and cladding, therefore these bubbles were not entrapped during the core melt casted on the cladding melt. They are entrapped during convection of the

composite glass during the extrusion molding. Fig.12 (d) shows the third type of the defect: the core region was spread by the rhombus shape structure: the anisotropy material might be crystalline composed by core composition.

Finally, the strength of the fiber was evaluated. The short term minimum bending radius was less than 15 mm. The tensile strength of the fiber was measured 5 times using Shimadzu AG-IS(50N) Autograph. The result showed values in the range of 453-496 MPa. The prepared fiber has higher tensile strength than that of previously reported [27], and had enough strength for handling and practical applications.

1.5 Conclusion

I successfully prepared ZBLAN fiber which has 0.22 of NA, and approximately 4-μm core diameter. The tensile strength and minimum bending radius are enough for practical use. The transmission loss of the fiber at 635 nm is 0.4 dB, however, further suppression of the loss can be achieved by eliminating defects in the fiber. I also ascertained that the source of the defects in the fiber are Pt particles, bubbles, and crystalline in the core. These defects can be suppressed by: improving the raw-material and the casting process, and adjusting the glass compositions.

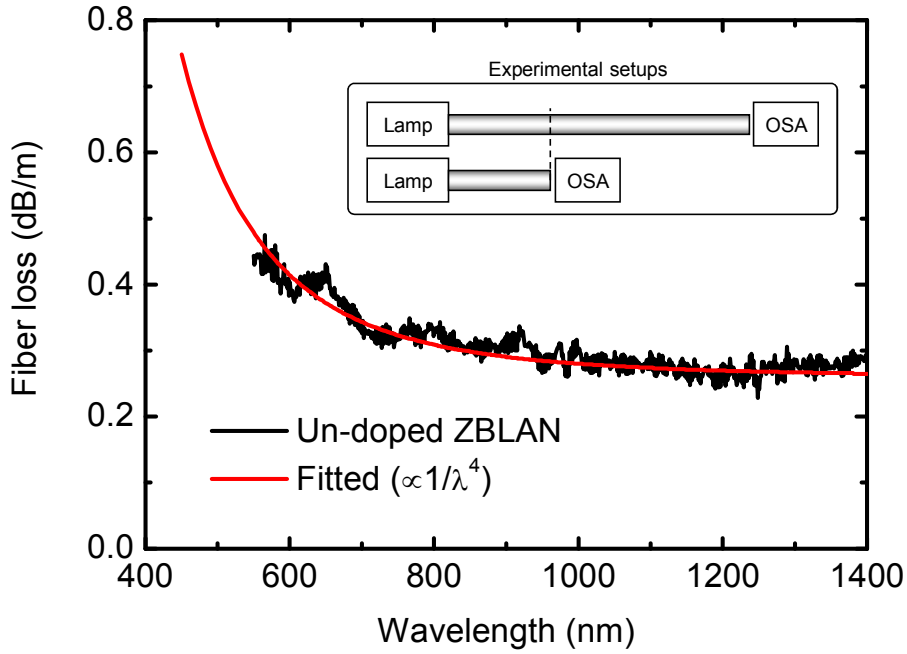

Fig. 11. Back ground loss of un-doped ZBLAN fiber on visible-NIR region.

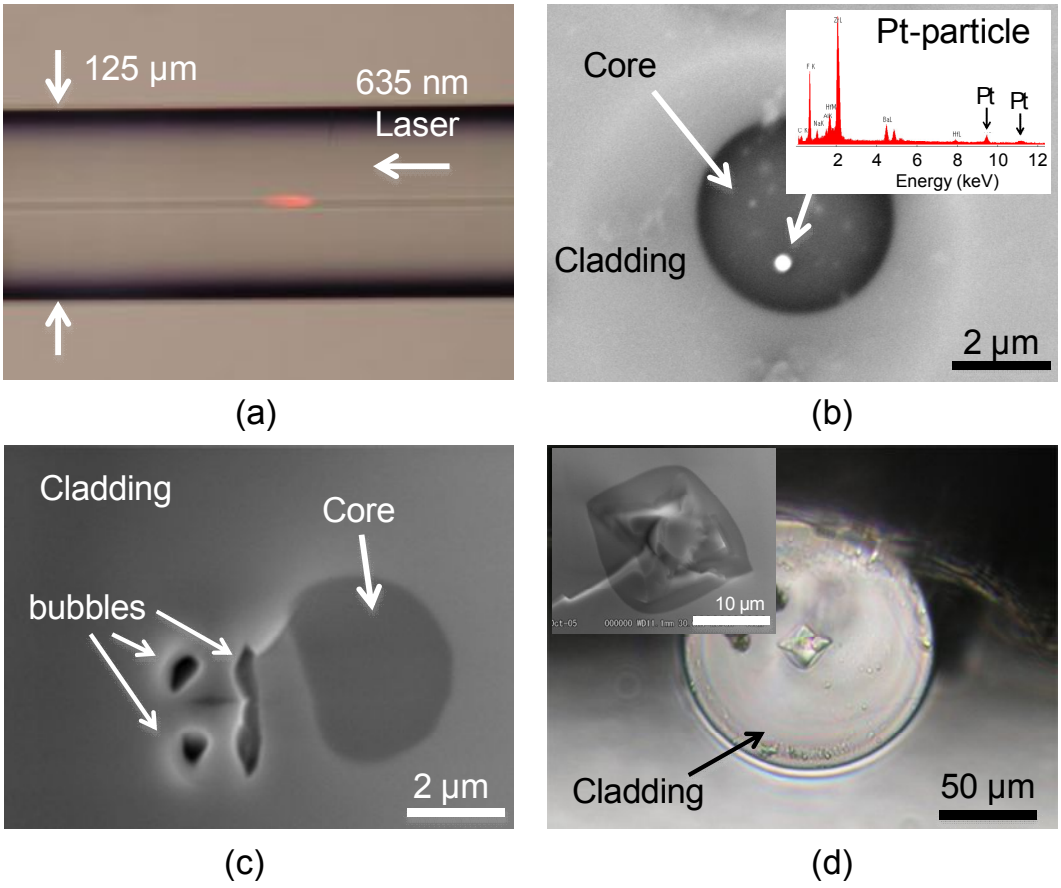

Fig. 12. Defects in fluoride fiber. (a) side view of blight spot while 635 nm laser was coupled into the fiber core. (b) Back scattered electron image of cross section of defect en by cleaving and etching. The composition of white spot was identified Pt. (c) distortion of core shape caused by bubble. (d) Optical microscope image of bright spot exposed by cleaving. The inset figure shows SEM image of the core.

References

1. S. Shibata, M. Horiguchi, K Jinguji, S. Mitachi, T. Kanamori and T. Manabe, Electronics Letters **17**(21), 775 (1981).
2. Y. Hatefi, N. Shahtahmasebi, A. Moghimi, and E. Attaran, Journal of Rare Earths **29**(5), 484 (2011).
3. R. M. Macfarlane, F. Tong, A. J. Silversmith, and W. Lenth, Applied Physics Letters, **52**(16), 1300 (1988).
4. J. Nakanishi, Y. Horiuchi, T. Yamada, O. Ishii, M. Yamazaki, M. Yoshida, and Y. Fujimoto, Optics Letters **36**, 1836 (2011).
5. S. D. Jackson, Electronics Letters **37**(13), 821 (2001).
6. H. Toebben, Electronics Letters **28**(14) 1361 (1992).
7. J. S. Sanghera and I. D. Aggarwal, Journal of the American Ceramic Society **76**(9), 2341 (1993).
8. J. L. Adam, Journal of Fluorine Chemistry **107**, 265 (2001).
9. M. Saad, in Passive Components and Fiber-Based Devices, B. Pal, ed., Vol. 8307 of Proceedings of SPIE (Optical Society of America, 2011), paper 83070N.
10. J. Nakanishi, Y. Horiuchi, T. Yamada, O. Ishii, M. Yamazaki, M. Yoshida, and Y. Fujimoto, Optics Letters **36**, 1836 (2011).
11. Hideyuki Okamoto, Ken Kasuga, Yoshinori Kubota, Natsuya Nishimura, Hiromi Kawamoto, Koichi Miyauchi, Yasuhiko Shimotsuma, and Kiyotaka Miura, Optics Express **21**, 22043 (2013).
12. S. Mitachi, S. Shibata and T. Manabe, Electronics Letters **17**, 128 (1981).

13. S. Mitachi, T. Miyashita and T. Manabe, Physics and Chemistry of Glasses **23**(6), 196 (1982) .

14. S. Mitachi, T. Miyashita and T. Kanamori, Electronics Letters **17**, 591 (1981).

15. D. C. Tran, C. F. Fisher and G.H. Sigel Jr, Electronics Letters **18**, 657(1981).

16. Y. Ohishi, S. Sakaguchi and S. Takahashi, Electronics Letters **22**, 1034 (1986)

17. Hiromi Kawamoto, Yoshinori Kubota, Natsuya Nishimura, and Akira Sakanoue, US Patent 5308371

18. P. W. France, PhD Thesis, Whiffield University (1987).

19. M. Robinson, R. C. Pastor, R. R. Truk, D. P. Devor, M. Braunstein and R. Braunstein, Materials Research Bulletin **15**, 735 (1980).

20. PS Christensen, P. LeGall, G. Fonteneau, J. Lucas. JY Boniort,1. Leboucq, D. Tregoat and H. Poigant, in Proc. 5th Int. Symp. on Halide Glasses, Shizuoka, Japan p. 113 (1988).

21. D.Tregoat, G.Fonteneau and J. Lucas, Materials Research Bulletin **20**, 179 (1985).

22. T. Nakai, Y. Mimura, H. Tokiwa, and O. Shinbori, Journal of Lightwave Technology, **LT-4**(1), 87 (1996).

23. S.F. Carter, P.W. France, M.W. Moore and E.A. Harris, Physics and Chemistry of Glasses **28**, 22 (1987)

24. P.W France, M.G. Drexhage, J.M. Parker, M.W. Moore, S.F. Carter, and J.V. Wright, Fluoride Glass Optical Fibres, Blackie, Glasgow, 1990

25. M. Poulain and C. Maze, Chemitronics **3**, 77 (1988)

26. K.Miura, I. Masuda, K. Itoh, and T. Yamashita, Materials Science Forum **67&68**, 335-340 (1991)

27. Schneider, Hartmut W., A. Schoberth, and A. Staudt, Glastechnische Berichte 60, 205 (1987)

28. M. Robinson, Journal of Crystal Growth **75**, 184 (1986)

Chapter 2

Visible-NIR broadband tunable Pr^{3+} doped fiber laser pumped by a GaN LD

2.1 Introduction

Visible and near-infrared (NIR) light sources can be widely used for many applications, such as laser TVs, laser projectors, optical diagnostic systems, and bio-medical laser microscopes. An ideal light source for these applications is a compact wide-band tunable laser that covers the visible to NIR regions. Optical parametric oscillators and super-continuum lasers, for example, can cover the wavelength range; however, these systems are large, complicated, and expensive.

As it shows many emission bands in these wavelength ranges [1], we have focused on Pr^{3+}-doped ZBLAN fiber (PDF) as a candidate for a wide-band tunable laser medium. A visible ASE light source was also demonstrated [2] and it shows blight visible emission as shown in Fig.1. The fluorescence spectrum, ground state absorption (GSA) spectrum, and excited state absorption (ESA) spectrum from $^1G_4$ of Pr^{3+}-doped ZBLAN glass are shown in Fig.2 [2,3]. Although fewer absorption bands occur around the 500–550 and 600–750 nm regions, seamless tunable laser operation has not been obtained over these bands [4–6]. We assume that the primary reason for the restricted tunable range was an excess cavity loss due to high background loss caused by redundant long fluoride fibers, for example, 0.70 dB/m at 450 nm and 0.35 dB/m at 635 nm.

In addition, GaN blue laser diodes (LDs) have recently been considered as a next-generation pumping source for Pr^{3+}-doped solidstate lasers [7–11]. Because of the high

absorption cross section of Pr^{3+} ions around 442 nm, PDF can perfectly absorb a blue pump laser even at less than 10 cm. Thus, we can use a short fiber for the laser to suppress background loss.

In this study, we set up a low-loss tunable laser cavity to achieve continuous wave (CW) wide-band tunable laser operation and clarify the maximum tunable range of a GaN-LD-pumped PDF laser from the visible to the NIR.

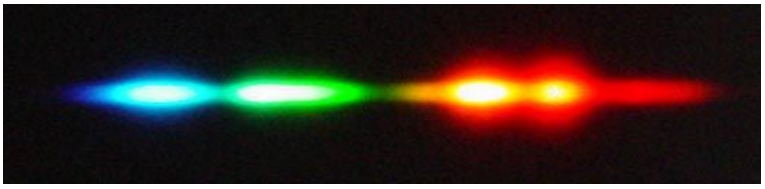

Fig. 1. Amplified spontaneous emission from Pr^{3+} doped fiber dispersed by prism.

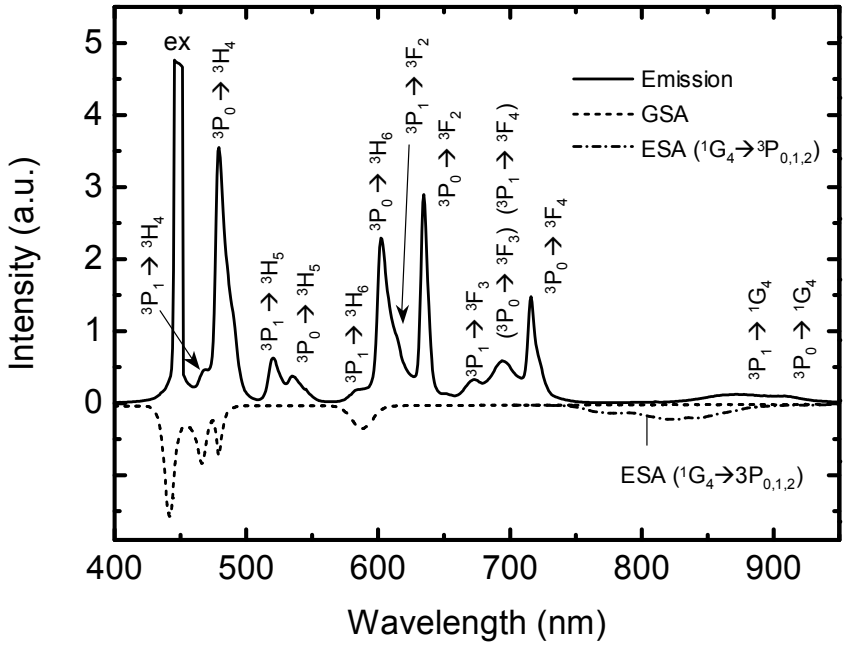

Fig. 2. Fluorescence spectrum and absorption spectra of Pr^{3+}:ZBLAN glass.

2.2 Experimental setup

We prepared a PDF with Pr^{3+} concentration of 3000 wt-ppm having a core diameter of 3.8–3.9 μm, cladding diameter of 125 μm, and numerical aperture of 0.22. The molar-percentage composition of the core glass is: ZrF_4(53.00)–BaF_2(22.00)–LaF_3(2.19)–YF_3(2.00)–AlF_3(3.50)–NaF(17.00)–PrF_3(0.31), abbreviated to Pr:ZBLAN. We used a transverse multimode 448-nm GaN LD (Nichia NDB7112E) as a pump source. The absorption coefficient of the PDF was 0.20 cm^{-1} at 448 nm.

Fig.3 shows the experimental setup of the tunable fiber laser system. The pump coupling optics was constructed of two aspherical lenses and a cylindrical lens pair. We prepared three dichroic mirrors at the pump side for blue–green, orange–"deep-red," and NIR laser operation: 448 nm AR/470–570 nm HR, 448 nm AR/520–735 nm HR, and 448 nm AR/740–1000 nm HR, respectively. The opposite end of the fiber was cleaved at 10º to suppress Fresnel reflection less than −50 dB. We also prepared two aspherical lenses (NA = 0.53) with different AR coatings (400–600 nm, 600–1000 nm) between the angle-cleaved fiber end and the prism. The emission from the PDF was dispersed by a prism with a MgF_2-AR coating. The laser oscillation wavelength was selected by rotating a broadband HR mirror. The round-trip prism reflection loss, which was averaged by two polarizations, was 0.8 dB from 448 to 974 nm. Therefore the corresponding output coupling ratio was 17%. The laser wavelength was measured using an ANDO AQ6315A optical spectrum analyzer (OSA) by monitoring one of the surface reflection of the prism.

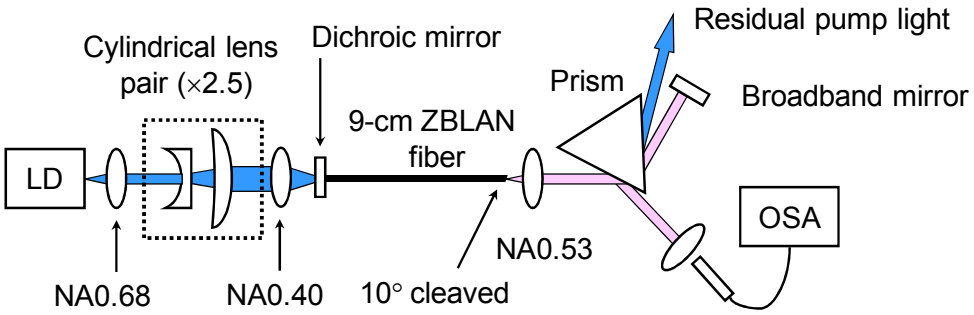

Fig. 3. Experimental setup of tunable fiber laser.

2.3 Results and discussion

First, we estimated the pump-coupling efficiency of an undoped ZBLAN fiber having the same fiber parameters as the PDF. The measured maximum coupled pump power into the un-doped fiber core was 252 mW, while the incident pump power to the fiber was 460 mW. The surface flatness and the angle of the cleaved fiber ends were confirmed for each cleaving to achieve a low-loss cavity, since the pump coupling efficiency and cavity loss depended heavily on the condition of the fiber ends. In addition, the quality of the surface and AR coating of the aspherical lens used in the laser cavity also greatly affected the width of the laser tunable range. We used an aspherical lens of 40-scratch/20-dig grade (MIL-O-13830A specification) in the laser cavity.

When we pumped the PDF at maximum pump power, tunable laser oscillation over a 300-nm range was achieved from the 9-cm PDF. Fig.4 shows the seamless tunability of the PDF laser (drawn with a 5-nm interval) within the emission band of Pr^{3+}-doped ZBLAN fiber. The tunable ranges and the corresponding transitions are shown in Fig.5 and Table 1. The total tunable range of the PDF laser was wider than that of conventional Ti:sapphire lasers (650–1100 nm) in the wavenumber. This is the first report of seamless tunable laser operation for transitions from multiple upper levels ($^3P_{0,1}$) to multiple lower levels ($^3H_{4,5,6}$, $^3F_{2,3,4}$, $^1G_4$) of a PDF laser. For the sake of simplicity, $^3P_1$ has been substituted for ($^3P_1$+$^1I_6$) in this letter [4].

The regions around 477, 588, and 1016 nm, in which laser oscillation were not observed, correspond to GSA: $^3H_4 \rightarrow {}^3P_0$, $^3H_4 \rightarrow {}^1D_2$, and $^3H_4 \rightarrow {}^1G_4$, respectively (Fig.2). The region around 830 nm corresponds to ESA, $^1G_4 \rightarrow {}^3P_{0,1,2}$ (Fig.2). Therefore, laser operation over these absorption bands is considered to be impossible. We could not obtain tunable laser operation from 497 nm to 515 nm, although neither GSA nor ESA exists there. We suppose that the gain was smaller than the cavity loss over the wavelength range. These tunable wavelength ranges

will be widened if we achieve lower cavity loss, for example, if the cavity mirror on the pump side is directly coated on the fiber end or the aspherical lens is replaced with one of higher surface quality.

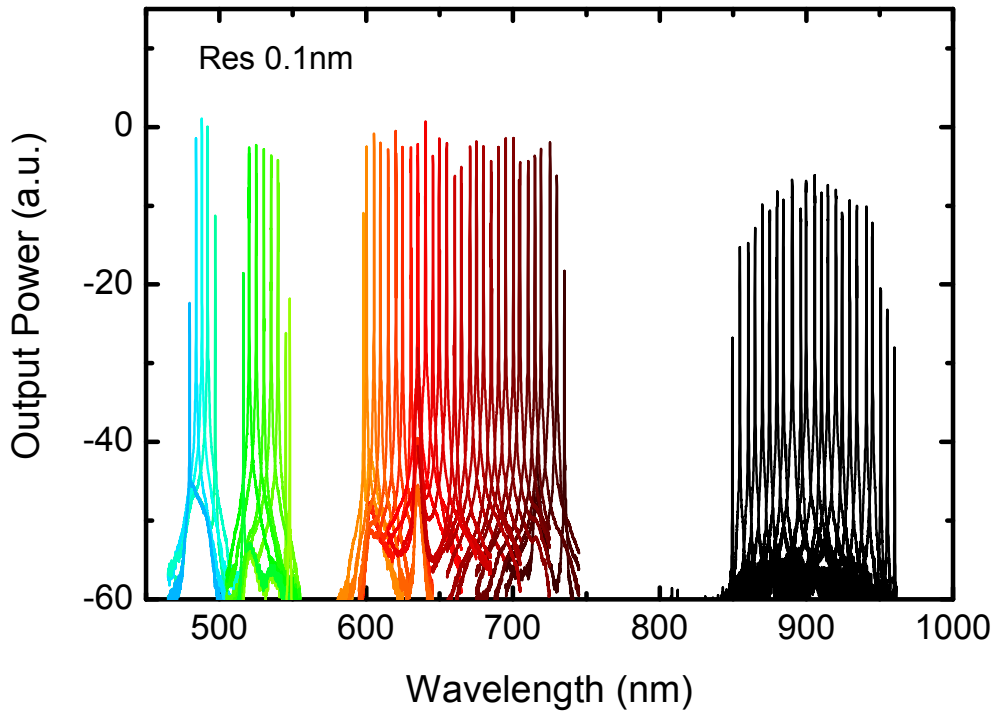

Fig. 4. Tunability of Pr^{3+} fiber laser pumped by a GaN LD.

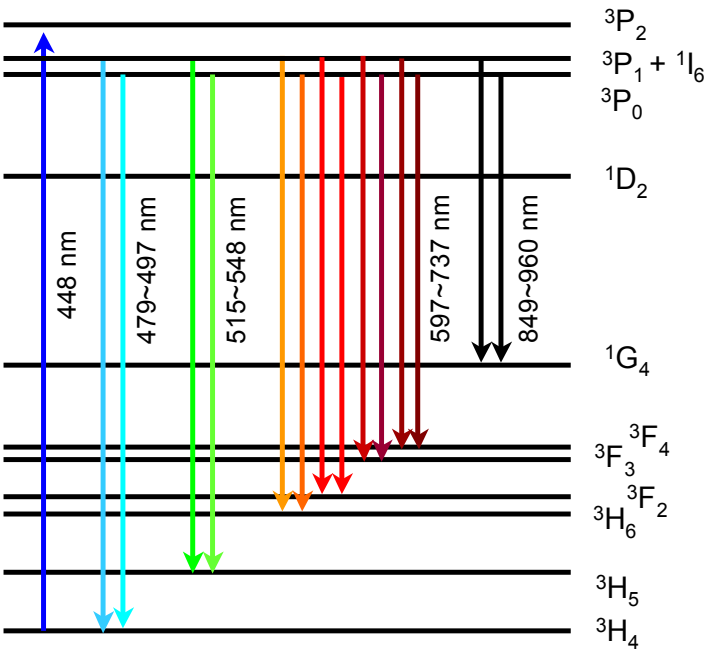

Fig. 5. Energy diagram of the Pr^{3+} ion and laser transitions for tunable laser.

Table 1. Tunable wavelength range and lasing transitions of Pr^{3+} fiber laser

	λ (nm)	Transitions	Δλ (nm)	Δν (cm^{-1})
PDF laser	479–497	$^3P_{1,0} \rightarrow {}^3H_4$	18	756
	515–548	$^3P_{1,0} \rightarrow {}^3H_5$	33	1169
	597–737	$^3P_{1,0} \rightarrow {}^3H_6, {}^3F_{2,3,4}$	140	3182
	849–960	$^3P_{1,0} \rightarrow {}^1G_4$	111	1362
		Total	302	6469
Ti:Sapphire laser	650–1100		450	6294

Although it seemed that the transitions from $^1D_2$ might contribute to widening the tunable range in the NIR region ($^3P_0 \rightarrow {}^1D_2 \rightarrow {}^3H_{5,6}, {}^3F_2$), we disproved that possibility as follows. Fig.6 shows the fluorescence spectrum of Pr:ZBLAN under excitation at 580 nm ($^3H_4 \rightarrow {}^1D_2$), measured by fluorescence spectrometer FP-6500 (JASCO) and PMA-11 (Hamamatsu). The largest emission was observed at 595 nm, but other emission corresponding to the transitions from $^1D_2$ (686, 795, 848 nm) were small enough to be negligible.

The maximum output powers and slope efficiencies are summarized in Fig.7 and Table 2. The horizontal axis in Fig.7 indicates the absorbed pump power estimated from the coupled pump power and residual pump power. Slope efficiencies of more than 29% were obtained except at 907 nm.

The threshold pump powers for 488 nm and 521 nm were larger than that of other wavelengths. In the case of 488 nm, GSA ($^3H_4 \rightarrow {}^3P_0$) makes the threshold large. In the case of 521 nm, the population of $^3P_1$ was reduced to below that of level $^3P_0$ ($\Delta 600$ cm^{-1}) by multi-phonon relaxation. Therefore, it is difficult to create a population inversion between $^3P_1$ and $^3H_5$.

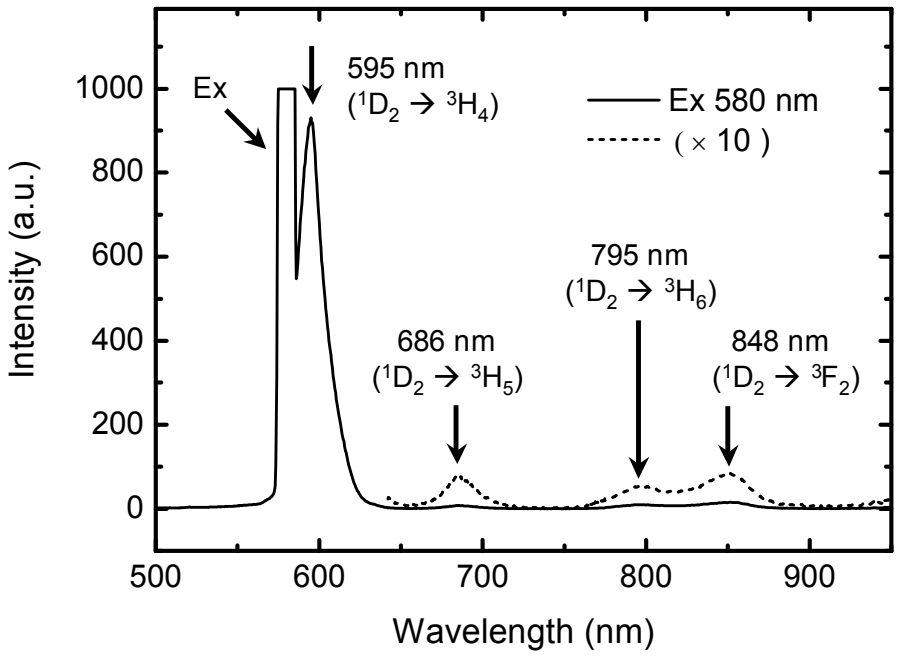

Fig. 6. Fluorescence spectrum of Pr^{3+}:ZBLAN under excitation at 580 nm.

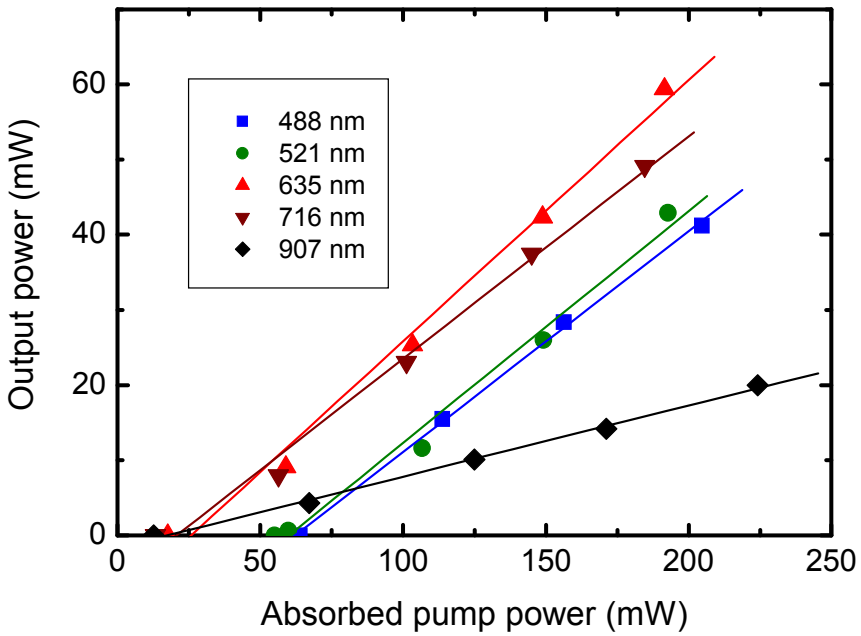

Fig. 7. Slope efficiencies for 9-cm PDF laser.

Table 2. Output powers and slope efficiencies of Pr^{3+} fiber laser.

λ (nm)	Maximum output power (mW)	Slope efficiency (%)	Threshold (mW)
488	42	29	62
521	43	31	60
635	59	35	26
716	49	30	21
907	20	9	17

2.4 Application for laser displays

Expanding a color gamut of displays is an important issue to achieve a natural vision. In recent years, laser-based displays have been dramatically developed because of the progress of visible solid state lasers [12, 13]. Primary colors of laser TV are generally used: InGaN lasers for blue, frequency-doubled Nd:YAG lasers or InGaN laser diodes for green, and AlGaInP laser for red. On the other hand, multi-primary color displays based on LCD, which contains additional primary colors to the standard three RGB colors, have been also proposed [14].

As mentioned in this chapter, the PDF laser can emit multi-color light on the visible range with one laser medium. The tunable ranges of the PDF laser are located the apex of a color gamut (Fig.8) then the total reproducible range covers most part of the visible range. If tunable lasers are used as primary colors for display, the color gamut can be controlled dynamically. Additionally, the compact wavelength tuning method for PDF laser, which is achieved by mirrors located in the fiber end with variable air gaps, has been successfully demonstrated [15]. The technology combining PDF laser and compact tunable cavity enables the color gamut of displays to be expanded.

2.5. Conclusion

I demonstrated CW tunable PDF laser operation over a 300-nm range (479–497, 515–548, 597–737, and 849–960 nm) pumped by a single GaN LD from a single 9-cm PDF. The total tunable range is 6469 cm^{-1}, which was wider than that of conventional Ti:sapphire lasers. The revealed ultra-wide tunability of PDF lasers is useful for laser TVs, biomedical applications, and other uses. Lasers in the cyan–green region are significant for expanding the color

reproduction range of laser TVs and laser projections. The wide tunablitiy of PDF lasers also has potential for short pulse generation at visible wavelengths.

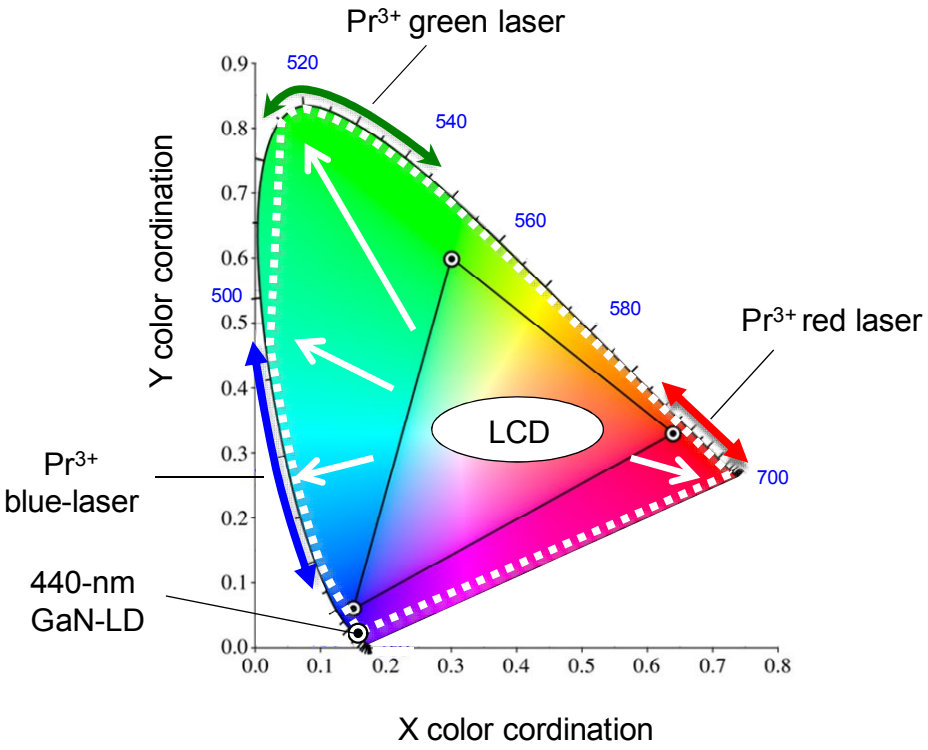

Fig. 8. Color gamut reproduced by Pr^{3+}: ZBLAN lasers. The wider color range can be reproduced by only one gain medium, compared with conventional liquid crystal display (LCD).

References

1. R. G. Smart, D. C. Hanna, A. C. Tropper, S. T. Davey, S. F. Carter, and D. Szebesta, Electronics Letters **27**(14), 1307 (1991).
2. H. Okamoto, K. Kasuga, I. Hara, Y. Kubota, Electronics Letters **44**(23), 1346 (2008).
3. H. M. Pask, A. C. Tropper, and D.C. Hanna, Optics Communications **134**, 139 (1997)
4. J. Y. Allain, M. Monerie, H. Poignant, Electronics Letters **27**(2), 189 (1991).
5. Ping Xie and T. R. Gosnell, Optics Letters **20**(9), 1014 (1995)
6. M. Zeller, H. G. Limberger, and T.Lasser, IEEE Photonics Technology Letters **15**(2) ,194 (2003)
7. A. Richter, E. Heumann, E. Osiac, G. Huber, W. Seelert, and A. Diening, Optics Letters **29**(22), 2638 (2004)
8. U. Weichmann, J. Baier, J. Bengoechea, and H. Moench, in CLEO/Europe and IQEC 2007 Conference Digest, (Optical Society of America, 2007), paper CJ5_1
9. P. Camy, J. L. Doualan, R. Moncorgé, J. Bengoechea, and U. Weichmann, Optics Letters, **32**(11), 1462 (2007)
10. A. Richter, E. Heumann, G. Huber, D. Parisi, and M. Tonelli, in Advanced Solid-State Photonics, OSA Technical Digest Series (CD) (Optical Society of America, 2008), paper MB2.
11. F. Cornacchia, A. Di Lieto, M. Tonelli, A. Richter, E. Heumann, and G. Huber, Optics Express **16**(20), 15932 (2008)

12. Jun Someya, Yoko Inoue, Hideki Yoshii, Muneharu Kuwata, Shuichi Kagawa, Tomohiro Sasagawa, Atsushi Michimori, Hideyuki Kaneko, and Hiroaki Sugiura, SID Symposium Digest of Technical Papers **37**(1), 1134 (2006)
13. Kishore V. Chellappan, Erdem Erden, and Hakan Urey, Applied Optics **49**, F79 (2010)
14. Hui-Chuan Cheng, Ilan Ben-David, and Shin-Tson Wu, Journal of Display Technology, **6**, 3 (2010)
15. Ortwin Hellmig, Stefan Salewski, Arnold Stark, Jörg Schwenke, Peter E. Toschek, Klaus Sengstock, and Valery M. Baev, Optics Letters **35**, 2263-2265 (2010)

Chapter 3

Efficient visible all-fiber laser: Splicing fluoride glass fiber to end coated silica fiber

3.1 Introduction

Fluoride glass fiber is widely known as a material that is transparent from the ultraviolet (UV) to the mid-infrared region. Several rare-earth ion-doped fluoride fiber lasers operating in that wavelength region have been reported [1–7]. Recent research has focused on visible fluoride fiber lasers pumped by a gallium nitride laser diode (GaN-LD) [8–11] because of the increased output power of GaN-LDs.

Most fluoride fiber laser resonators reported had a dichroic mirror attached to the end of the fiber, and a lens focused the pump light into the fiber core; thus, the ends of the fluoride fiber were exposed to the air. Strength degradation in ZrF_4-based fluoride fiber during a damp heat test has been reported [12]; therefore, this air gap at the end of the fluoride fiber might reduce its long-term reliability. A gapless all-fiber laser using fluoride fiber would significantly improve the reliability. Researchers have used techniques for splicing fluoride fiber to silica fiber [13–19], predominantly for optical amplifiers. An all-fiber laser will be achieved if these techniques are used to splice fluoride fiber to a fiber Bragg grating (FBG) or a wavelength-division multiplexing (WDM) coupler.

Previous studies used either an FBG or a WDM coupler to set up an all-fiber laser from the visible to the near-infrared region. For the FBG, they used a Ge-doped fiber to write a Bragg grating in its core. Researchers recently suggested that UV-visible light could generate a Ge-related defect [20–22]. Although laser operation using an FBG was reported around 605 nm

[23], pumping and laser operation at shorter wavelengths would be problematic, if a Ge-doped silica fiber device is used in an all-fiber laser.

In this chapter, We proposed and demonstrated the quasi-fusion splicing between silica fiber and fluoride fiber, which have different softening temperature (T_s) in first phase of experiment. After that, we constructed an all-fiber laser by using the spliced structure of Pr^{3+} doped ZBLAN fiber and end coated silica fiber, considering the difference between the softening temperatures of the ZBLAN and silica fibers. The concept of laser cavity proposed here is shown in Fig.1 Then we demonstrated an all-fiber laser operated at 521 nm, which corresponds to the peak wavelength of the Pr^{3+} fluorescence spectrum in the green region and is desirable for laser projectors and laser TVs.

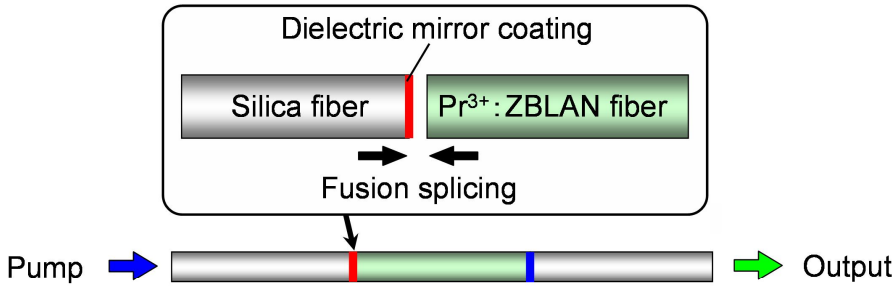

Fig. 1. Concept of all-fiber laser resonator.

3.2 Quasi-fusion splicing fluoride glass fiber and silica fiber

At first, we prepared two fibers, ZBLAN fiber and silica fiber, which had the same cladding diameter 125 μm, in order to optimize the splicing condition. The UV coating of fluoride fiber was removed by immersing it into acetone and was tone off. After that, the fluoride fiber was cleaved by using YORK FK-11 fiber cleaver. The silica fiber to be spliced was also cleaved by Fujikura CT-20 fiber cleaver. Both cleaved fiber ends were cleaned with ultrasonic cleaner containing isopropyl alcohol to remove fragments of fiber.

In order to splice these two fibers, we used Fujikura FSM-40F programmable arc fusion splicer operated at 1.37 version firmware. The motion of motors of FSM-40F was controlled by externally connected computer.

Due to the fact that fluoride glass fiber has much lower softening temperature (T_s<500°C) compared with silica glass (T_s >1400°C), the splicing condition for conventional silica fibers could not be applied. In order to splice fluoride fiber to silicate fiber directly, the arc power of FSM-40F was set to a minimum value of -42 bit. Furthermore, only silica fiber was heated by arc discharge to suppress the excess thermal effect to the fluoride fiber.

The detailed procedure of the splicing is shown in Fig.2. First, silica fiber and fluoride fiber were positioned opposite to each other, and the gap of the two fibers was set to 20 μm (Fig. 2 (a)). After that, the two fibers were moved 830 μm to Z-direction to recede fluoride fiber from the electrodes (Fig.2(b)). Then two fibers were XY-aligned by using 980 nm laser and ILX lightwave FPM8210H power meter to minimize the transmission loss (Fig.2(c)). Finally, the silica fiber was heated by pulse arc discharge for 500 ms (duty 33%) and was pushed toward the fluoride fiber 30μm (gap + 10 μm) (Fig.2(d)). Just after that, the pulse arc discharge was also applied for 2000 ms (duty 12.5%) to distress the splicing point (Fig.2(e)).

The off-set length Z during the splicing had a great influence for both deformation of fluoride fiber and insertion loss of splice point. Fig.3 shows images of splicing point arced at different Z values. The splicing point was closer to electrodes, the fluoride fiber was overheated and was deformed excessively. On the contrary, the fluoride fiber was not deformed when splice point was moved away from the electrodes: then the deformation of fluoride fiber can be controlled by the offset length Z.

The detail of the structure of splicing point was observed with SEM as shown in Fig.4. Only the ZBLAN fiber bulged during splicing, because the T_s of the silica glass is relatively higher than that of the fluoride glass (Fig.4(a)). The cross section of the splice point after tensile test revealed that fluoride fiber was deformed but was not sunk by silica fiber (Figs.4(b),(c)). Nevertheless the splice point was broken after a tensile test, the fragments of fluoride fiber were strictly adhered on the surface of silica fiber (Fig.4(d)). The analysis of the mechanism of adhesion between silica glass and fluoride glass is a future issue.

Finally, splice points were fixed into the SUS304 tube (D_{in} 0.45 × D_{out} 0.50 × L10 mm) with epoxy resin (ThreeBond 2212B) which have small thermal expansion coefficient (4.5×10^{-5} / °C).

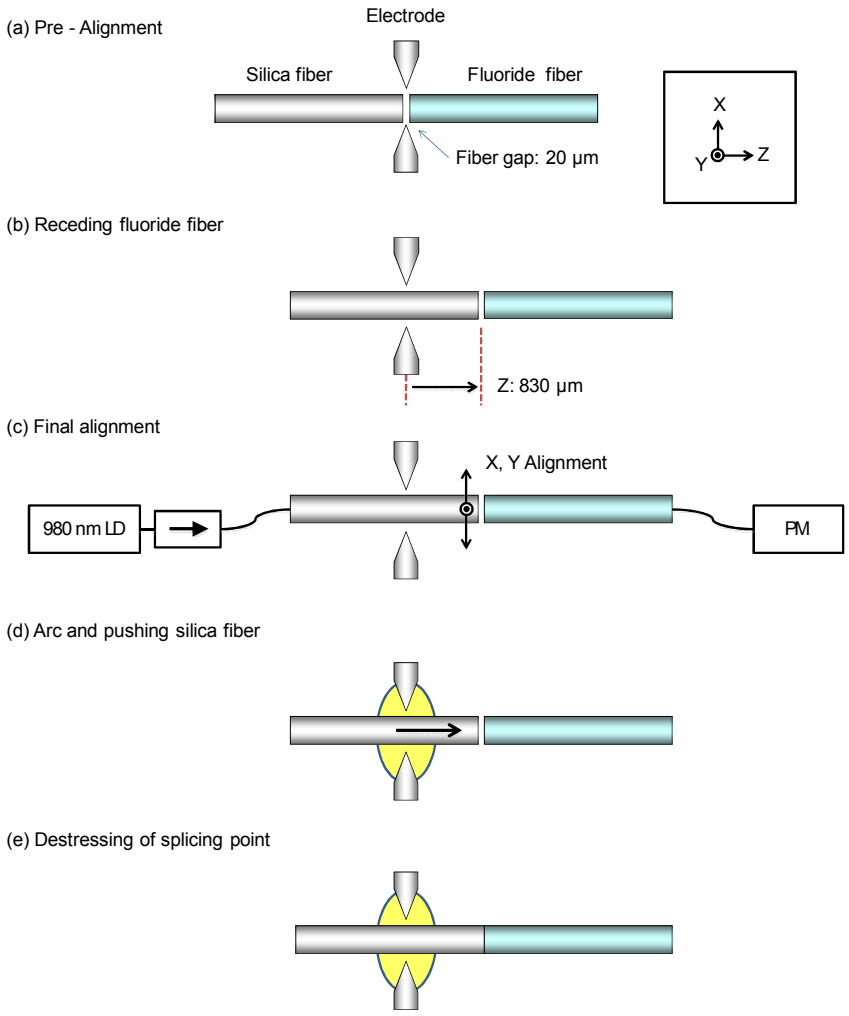

Fig. 2. Procedure of quasi-fusion splicing between silicate fiber and fluoride fiber

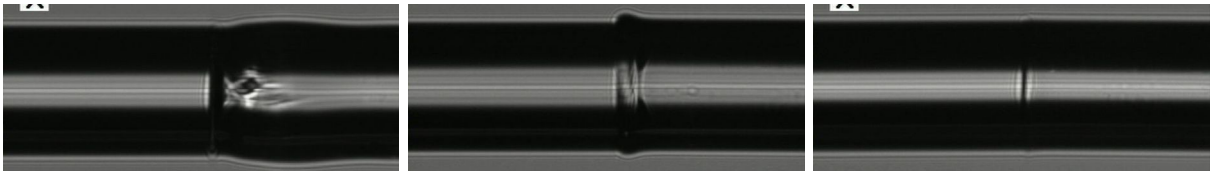

(a) Z = 700 μm (b) Z = 830 μm (c) Z = 960 μm

Fig. 3. Optical images of splicing points at various offset length Z. As splicing point got close to electrode (Z = 0), the end of fluoride fiber tended to be distorted. The better tensile strength was obtained (b), while splice point (a) and (c) were too fragile to handle.

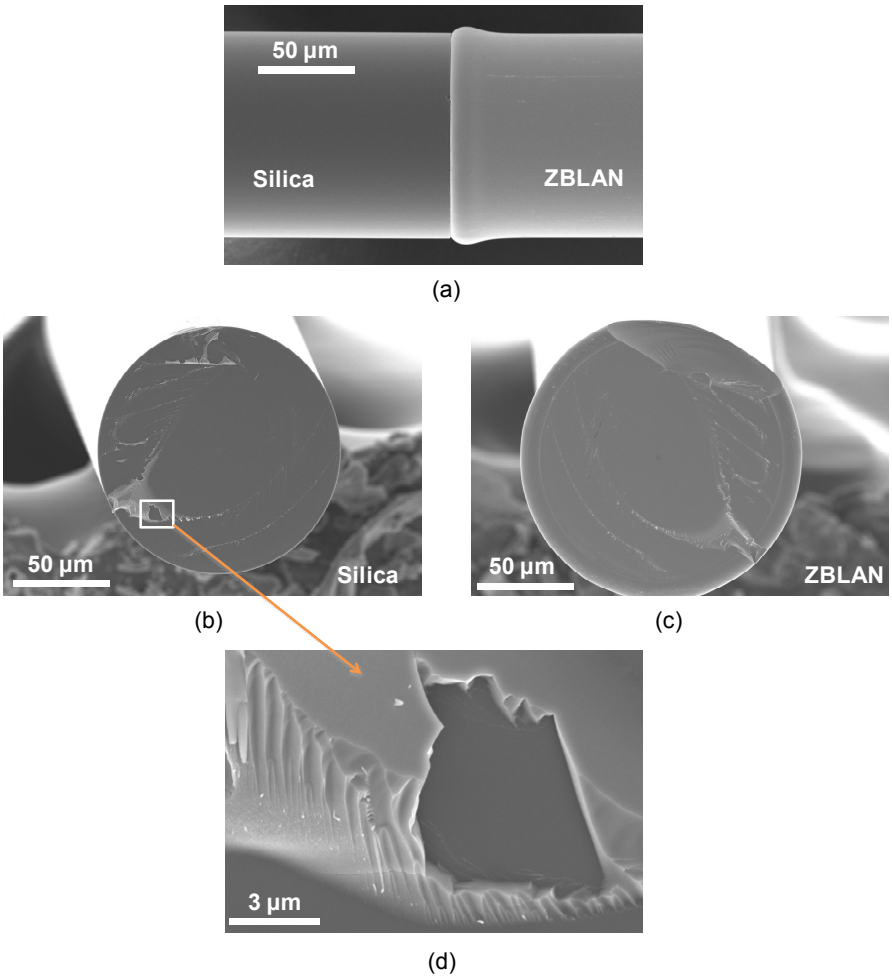

Fig. 4. SEM images of splicing point between silica and ZBLAN fiber. (a) side view of splicing point, (b) cross section of silica fiber after tensile test, (c) corresponding cross section of fluoride fiber, (d) enlarged image of (b). Fluoride glass is strictly adhered on the silica fiber.

3.3 Experimental setup

First, we prepared a PDF having a core diameter of 3.6 μm, cladding diameter of 125 μm, and numerical aperture of 0.22. The molar percentage composition of the core glass was ZrF_4(53.00)–BaF_2(22.00)–LaF_3(2.19)–YF_3(2.00)–AlF_3(3.50)–NaF(17.00)–PrF_3(0.31). The measured absorption coefficient of the PDF at 448 nm was 0.20 cm^{-1}. The glass transition temperature (T_g) and the crystallization temperature (T_x) of the ZBLAN glass were 273 °C and 358 °C, respectively. The T_s of ZBLAN glass was approximately 320 °C [24].

Next, in order to make silica fibers with dielectric coating, we also prepared silica fiber having a core diameter of 3.5 μm, cladding diameter of 125 μm, and numerical aperture of 0.20. We cleaved the ends of the silica fibers at less than 0.4º, as close as possible to 0º. Then, we used the ion-assisted deposition process to coat the dielectric mirror on the cleaved surface of the silica fiber. The dielectric mirrors coated were designed to suppress all the laser oscillations from 470 to 730 nm except those in the 521-nm band, because the Pr^{3+}-doped ZBLAN glass has several emission bands at visible wavelengths. The pump-side coating transmitted 440–450-nm pump light and reflected over 99.5% of the 521-nm light. The reflectance of the output-side mirror was experimentally optimized to 85% for the 521-nm light. The thicknesses of the pump-side and output-side dielectric mirrors were 2.5 and 1.5 μm, respectively. Although these fibers serve as multimode fibers at visible wavelengths, we chose these fiber parameters to maximize the coupling pump power from our pump laser emitted by multimode GaN-LDs (Nichia NDB7112).

In order to splice the fluoride fiber to the end coated silica fiber, we heated the silica fiber to a temperature above the T_s of the ZBLAN glass, and then immediately pressed it against the ZBLAN fiber as mentioned in Section 3.2. The offset splicing (Z = 830 μm) for fluoride fiber

was also useful for end coated silica fiber to avoid the damage to the coating caused by arc discharge.

We spliced the pump-side coated fiber to a 13-cm-long PDF and the output-side coated fiber to the opposite side of the PDF as shown in Fig. 1. In this study, we refer to this piece of PDF, whose ends are spliced to coated fibers, as the PDF module. Fig. 5 shows the transmission spectra of the coated fibers before splicing and the PDF module. We used a halogen lamp with an ANDO AQ6315A optical spectrum analyzer (OSA) to measure the transmission spectra. The transmission loss of the PDF module was 1.0 dB at 635 nm, and its loss around 590 nm corresponded to the ground state absorption of Pr^{3+} ions ($^3H_4 \rightarrow {}^1D_2$).

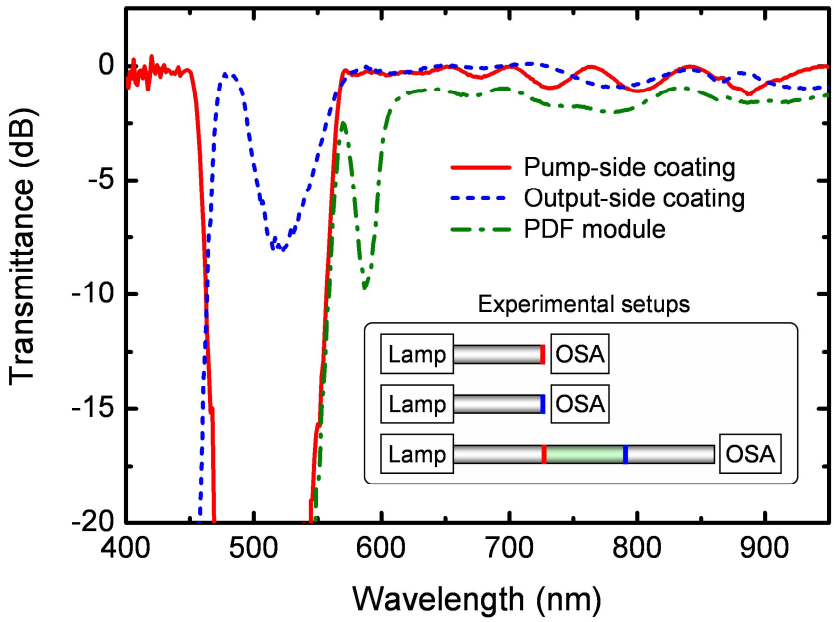

Fig. 5. Transmission spectra of end-coated silica fibers and PDF module. Inset shows experimental setups.

3.4 Result

Two GaN-LDs (442 and 448 nm) were used to pump the PDF module. Each elliptical beam from the GaN-LDs was shaped into a circular beam by using a different pair of cylindrical lenses [10]. Then, these two beams were combined by a polarization beam splitter and launched in the PDF module as shown in Fig.6. The optical power was measured by an Ophir 12A-P power meter. Before the laser experiment, we estimated the pump power coupled to the PDF by measuring the pump coupling ratio of the silica fiber: the measured maximum coupled pump power in the silica fiber core was 652 mW, whereas the pump power incident on the silica fiber was 1050 mW resulting in an efficiency of 62%.

Using the all-fiber laser resonator with the spliced structure, we successfully operated the laser at 521 nm as designed as shown in Fig.7. The input-output property of this 521-nm ZBLAN fiber laser was shown in Fig.8. We achieved a maximum laser power of 322 mW. The threshold pump power and the slope efficiency were 35 mW and 53%, respectively.

The inset of Fig. 8 shows the spectrum of the 521-nm PDF laser while its output power was 322 mW. The 10-dB bandwidth of this laser was 2.0 nm, which contributes more to suppressing the speckle contrast than a second-harmonic generation (SHG) green laser. The output power stability of the PDF laser was measured by a TTI TIA-525 O/E-converter and Tektronix TDS3014 oscilloscope. When the output power of the 521-nm laser was 322 mW, the peak-to-peak noise and the root-mean-square (RMS) noise under free-running conditions were 6.5% and 0.7% (0.1 Hz to 12.5 MHz), respectively.

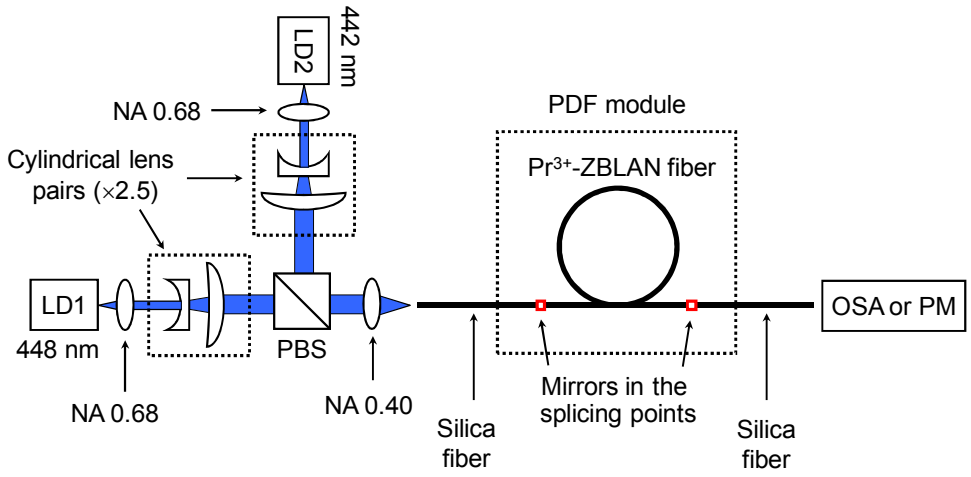

Fig. 6. Experimental setup for our 521-nm Pr^{3+} fiber laser.

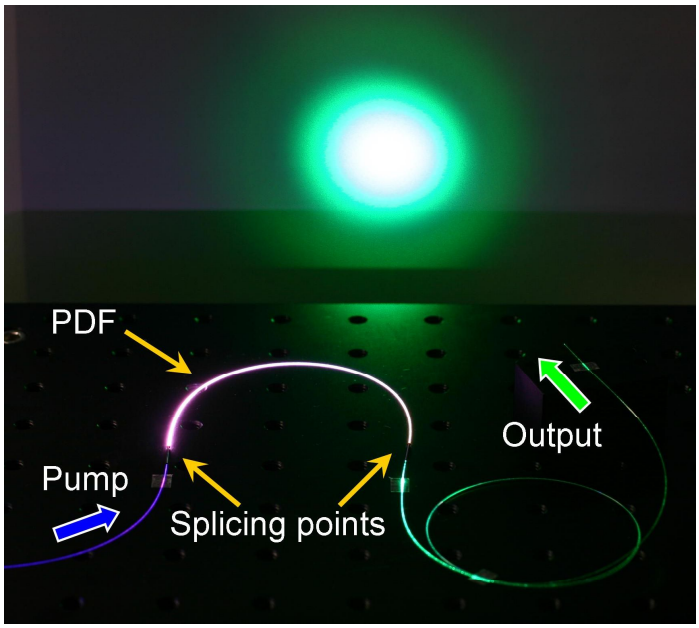

Fig. 7. Photograph of PDF module pumped by blue GaN-LDs. Dielectric mirrors are in the splicing point.

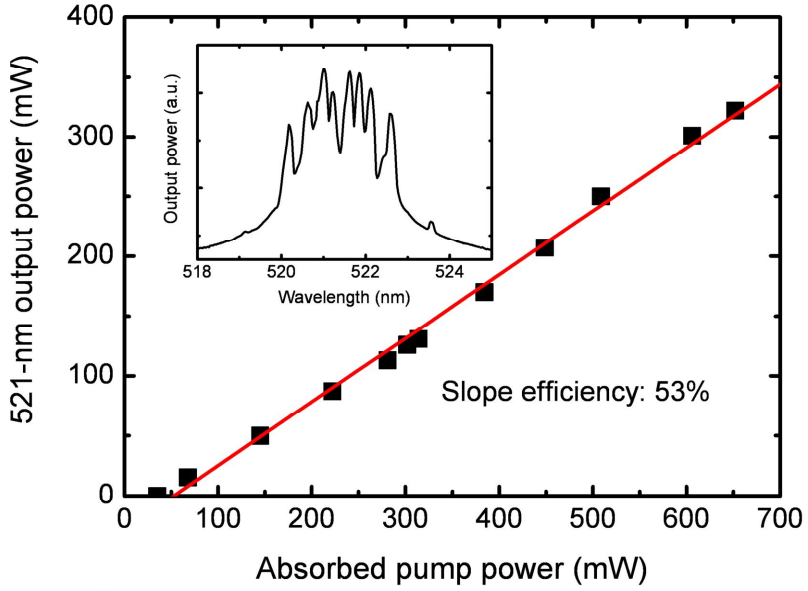

Fig. 8. Input and Output property of 521-nm Pr^{3+}:fiber laser pumped by GaN LDs. Inset shows the wavelength spectrum while laser output power was 322 mW.

Finally, we measured a bonding strength of the splicing point between the end-coated silica and ZBLAN fibers, and investigated the variation of the characteristics of the dielectric mirror coating on the silica fiber end before and after splicing. As a result of a tensile test of the pump-side splicing point, the maximum bonding strength of the splicing point was 70 MPa, despite the large difference between the coefficients of thermal expansion of the two different fibers.

Fig. 9 shows the optical microscope images of the fiber surface at the breaking point before splicing and after the tensile test. We confirmed that the fragment of fluoride fiber was directly adhered to the dielectric mirror, and the structure of the dielectric mirror coating on the end of the silica fiber remained unaffected, as shown by the perfect reflection of green light from the end of the silica fiber [Figs. 9(b), (b')]. We also measured the transmission spectra of the dielectric mirror coating spliced and broken after the tensile test by the experimental setup shown in Fig. 7; the spectra did not change. Although we increased the temperature of the dielectric mirror above the T_s of the ZBLAN glass during splicing, the dielectric mirror coating did not suffer any damage because of splicing.

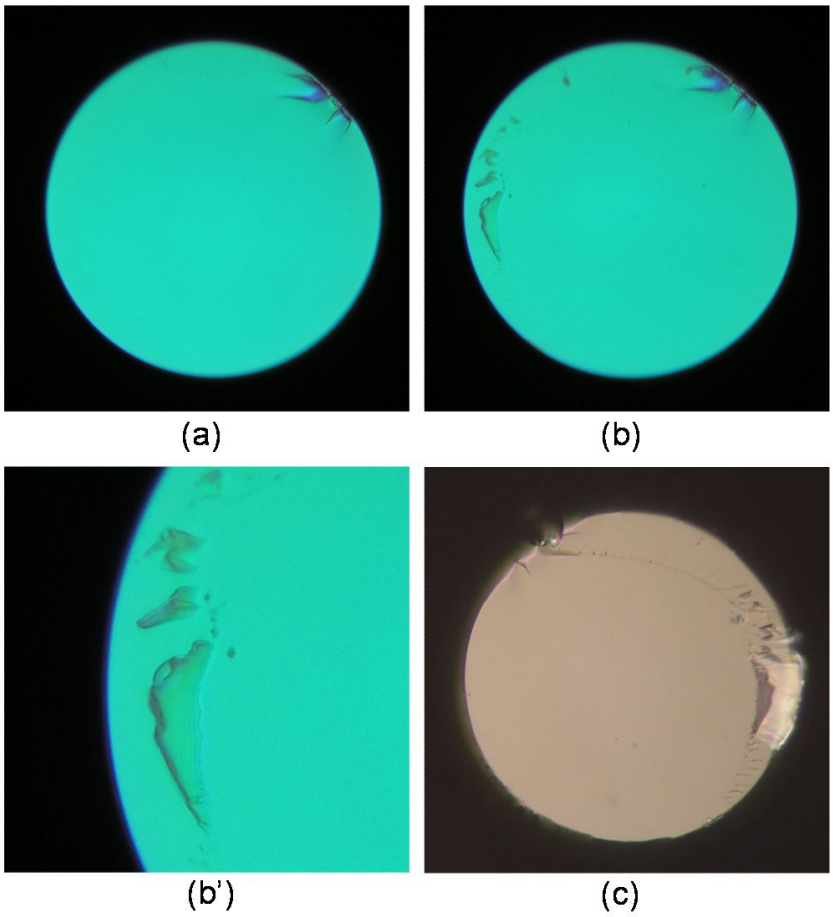

Fig. 9. Optical microscope images of cross sections of pump-side end-coated fiber and ZBLAN fiber: (a) end-coated fiber before splicing, (b) end-coated fiber spliced and broken after tensile test, (b') enlarged image of (b), and (c) PDF spliced and broken after tensile test

3.5 Discussion

As mentioned above, we demonstrated that it is possible to splice a ZBLAN fiber to end-coated silica fibers without causing any damage, and that the spliced structure serves as a laser resonator at visible wavelengths. Considering the internal laser power density at the output-side splicing point, the damage threshold of the splicing point was estimated above 21 MW/cm^2. These results indicated that an all-fiber laser that uses our spliced structure would be a potential candidate not only for UV-visible lasers but also for high-power lasers, such as large-mode-area fiber lasers and double-cladding fiber lasers. Furthermore, the reflection and transmission characteristics of our spliced structure was transverse-mode independent; thus it would be easy to construct a multimode fiber laser resonator.

The laser output power and the slope efficiency of the PDF module were comparable to the properties of a Pr^{3+}:$LiYF_4$ laser [25] despite significant PDF module loss. If we assume that the splicing loss at each splicing point to be 0.5 dB (corresponding to half of the PDF module loss at 635 nm), the maximum pump power launched at the core of the PDF and the maximum 521-nm output power are 581 mW and 361 mW, respectively, thus the actual slope efficiency is estimated to be 67%. The splicing loss of the PDF module was greater than that of a ZBLAN fiber spliced to a silica fiber without a dielectric mirror coating [14]. Further optimization of the splicing conditions is required to minimize the deformation of the ZBLAN fiber due to splicing. Recently, the splicing between fluoride fibers were also demonstrated with Vytran GPX 3400 splicer [26]: the splice loss of two different fluoride fibers, a single mode 9 μm core and a multimode fiber 85μm core fibers, were 0.1 dB and its splicing strength was 40 kpsi (276 MPa). Therefore fusion splicing technique would be a promising method to construct a cavity for fiber laser.

Our laser resonator did not require a Ge-doped fiber, which is essential for FBG; therefore, a dielectric mirror coated on the end of the pure-silica core fiber can be used for an all-fiber laser in the UV-visible region. Our splicing technique could be used for the splicing of two arbitrary fibers that have different T_s values, e.g., halide glass, bismuth glass, vanadium glass, or tellurite glass spliced to a silica fiber. This splicing technique would apply not only to reflectors placed at the splicing point but also to anti-reflection coatings with different material indices.

The PDF laser properties of transverse multimode output and wide laser bandwidth will contribute to reducing the speckle contrast of laser projectors and laser TVs. In addition, the PDF laser emits a stable CW output of a 322 mW without any active cooling. These are significant advantages over SHG lasers for practical applications.

For another application, we can substitute a WDM coupler for the spliced structure for broadband fiber sources such as superfluorescent fiber sources and amplified spontaneous emission light sources to intensify the output power [27,28].

3.6 Conclusion

We developed an all-fiber laser resonator by fusion splicing both sides of a PDF to end-coated silica fibers. The maximum output power and the slope efficiency of the 521-nm fiber laser were 322 mW and 53%, respectively. The slope efficiency is the highest value obtained for a green fiber laser. The characteristics of the dielectric mirror did not change after splicing; therefore, this technique of splicing two materials with different T_s values is practical for all-fiber lasers.

References

1. D. S. Funk, J. W. Carlson, and J. G. Eden, Electronics Letters **30**(22), 1859 (1994).
2. J. Y. Allain, M. Monerie, and H. Poignant, Electronics. Letters **26**(3), 166 (1990).
3. J. Y. Allain, M. Monerie, and H. Poignant, Electronics Letters **27**(2), 189 (1991).
4. K. Hirao, S. Todoroki, and N. Soga, Journal of Non-Crystalline Solids **143**, 40, (1992).
5. J. Y. Allain, M. Monerie, and H. Poignant, Electronics. Letters **26**(4), 261 (1990).
6. S. Tokita, M. Murakami, S. Shimizu, M. Hashida, and S. Sakabe, Optics Letters **34**, 3062 (2009).
7. J. Schneider, C. Carbonnier, and U. B. Unrau, Applied Optics **36**, 8595 (1997).
8. A. Richter, E. Heumann, E. Osiac, G. Huber, W. Seelert, and A. Diening, Optics Letters **29**(22), 2638 (2004).
9. U. Weichmann, J. Baier, J. Bengoechea, and H. Moench, in CLEO/Europe and IQEC 2007 Conference Digest, (Optical Society of America, 2007), paper CJ5_1.
10. H. Okamoto, K. Kasuga, I. Hara, and Y. Kubota, Optics Express **17**, 20227 (2009).
11. Y. Fujimoto, O. Ishii, and M. Yamazaki, Electronics Letters **46**(8), 586 (2010).
12. K. Fujiura, K. Hoshino, T. Kanamori, Y. Nishida, Y. Ohishi, and S. Sudo, in Optical Amplifiers and Their Applications, Vol. 18 of 1995 OSA Technical Digest Series (Optical Society of America, 1995), paper ThE4.
13. B. Srinivasan, M. Erlandsson, G. S. Feller, E. W. Mies, and R. K. Jain, in Optical Fiber Conference, OSA Technical Digest Series (OSA, 1997), paper TuB1.
14. Y. Kubota, and Y. Akasaka, "Recent progress of fluoride-based EDFA: Expanded gain bandwidth and practicality," presented at the Tech. Dig. Optoelectronics and

Communications Conf./Conf. Optical Internet (OECC/COIN), Yokohama, Japan, 14D4-1 (2004).

15. L. Pei, X. Dong, R. Zhao, C. Qi, R. Caspary, M. S. Kien, and S. Jian, Proc of SPIE **6781**, 67814O (2007).
16. M. M. Kozak, W. Kowalsky and R. Caspary, Electronics Letters **41**(16), 21 (2005).
17. M. Yamada, F. Hanawa, T. Kitoh, and T. Maruno, IEEE Photonics Technology Letters **14**(8), 906 (1992).
18. M. Karasek, Optics Communications, **107**, 235 (1994).
19. Y. Nishida, K. Fujiura, K. Hoshino, M. Shimizu, M. Yamada, K. Nakagawa, and Y.Ohishi, IEEE Photonics Technology Letters **11**(12), 1596 (1999).
20. J. Xie, T. Deng, J. Luo, and Q. Han, Journal of Wuhan University of Technology-Materials Science Edition **23**(6) (2008).
21. K. Médjahdi, F. Goutaland, A. Boukenter, and Y. Ouerdane, Journal of Non-Crystalline Solids **351**, 1835 (2005).
22. A. Anedda, C. M. Carbonaro, R. Corpino, and A. Serpi, Journal of Non-Crystalline Solids **280**, 281(2001).
23. M. Zeller, H. G. Limberger, and T. Lasser, IEEE Photonics Technology Letters **15**(2), 194 (2003).
24. Y. Hou, Y. Li, X. Chen, G. Zhang, and Y. Wang, Journal of Non-Crystalline Solids **260**, 54-58 (1999).
25. N. O. Hansen, A. R. Bellancourt, U. Weichmann, and G. Huber, Applied Optics **49**, 3864 (2010).

26. Mohammed Saad, Passive Components and Fiber-Based Devices VIII, edited by Bishnu P. Pal, Proc. Of SPIE-OSA-IEEE Asia Communications and Photonics, SPIE Vol. 8307, 83070N

27. L. A. Wang, C. T. Lee, and G. W. You, Applied Optics **44**, 77 (2005).

28. H. Okamoto, K. Kasuga, I. Hara, and Y. Kubota, Electronics Letters **44**(23), 1346 (2008).

Chapter 4

White light emitting fluoride glasses containing divalent Ytterbium ion efficiently excited at near UV light

4.1 Introduction

White light-emitting diodes (LEDs) have recently attracted interest as efficient light sources and have conventionally been fabricated with a yellow phosphor (YAG:Ce^{3+}) and blue GaN chips [1]. However, several problems with the light quality from these types of white LEDs have been reported, including poor color rendering, color shifts caused by changes in current, and an uncomfortable glare [2, 3]. Thus, much effort has been directed toward addressing these issues. Multicolor phosphor systems (e.g., red, yellow, green, and blue) excited with near-UV light have also been proposed [4]. However, mixing different color phosphors causes low luminous efficacy and undesirable luminescence because the light emitted from blue phosphors is internally absorbed by red-green phosphors [3, 4]. In order to avoid this "re-absorption", phosphors which have very weak absorption in blue regions and based on near-ultraviolet (UV) excitation are developed, such as yellow-emitting phosphors $(Ca_{1-x-y}, Sr_x, Eu_y)_7(SiO_3)_6Cl_2$ [5]. Single-phased multi-activators with co-doped materials capable of generating white light under UV excitation are also developed, which are based on the luminescence and energy transfer between multi-activators, such as Eu^{2+}/Mn^{2+} [6], Ce^{3+}/Mn^{2+} [7], Ce^{3+}/Eu^{2+} [8]. In contrast, Yb^{2+} doped crystalline host have been recently demonstrated as a green phosphor, such as Yb^{2+}:α/β-SiAlON [9, 10] .

Glass phosphors emitting white luminescence have also been investigated, containing Ag/Eu^{3+} [11], Cu^{+}/Eu^{3+} [12], Cu^{+}/Sm^{3+} [13], Ce^{3+}/Sm^{3+} [14], Tb^{3+}/Sm^{3+} [15], Mn^{2+} without rare earth cation [16] in various glass. The glass phosphors can be formed in platelike shape directly without epoxy-resin, therefore they have advantages for practical use of LED to avoid aging of the coating layer of LED under long-term UV irradiation or thermal degradation [11, 12, 17].

On the other hand, Verwey et. al demonstrated Yb^{2+}-doped SrF_2–YF_3–AlF_3–MgF_2 (SYAM) fluoride glass which emits wide-band luminescence at visible wavelengths; however, its peak excitation wavelength is less than 250 nm, and the glass exhibits a grayish color as a result of the melting process in a reductive atmosphere [18]. While this glass phosphor has high quantum efficiency (QE), the excitation wavelength (deep-UV) is much shorter than visible wavelengths; thus, thermal losses corresponding to Stokes shifts are unavoidable in visible applications. Moreover, compositions of Yb^{2+}:fluoride glasses for white LED have not been investigated yet. If Yb^{2+}:fluoride glass can be efficiently excited at near UV light, re-absorption less, epoxy resin free, novel white LED will be realized.

We investigated the potential use of Yb^{2+}:fluoride glasses excited with near-UV light in visible applications. First, suitable fluoride glass compositions containing highly reduced Yb ions that maintain high transmittance even under a reductive atmosphere were identified. Chloride ions were then incorporated into fluoride glasses to intensify white emissions, and the QEs of the modified glasses were evaluated.

4.2 Experimental

Three fluoride glass systems were prepared with the starting compositions in the mole percentages as listed in Table 1. In addition, three types of glass were prepared for each glass system: (1) YbF_3-doped glass (x = 0.2) melted under a reductive atmosphere, (2) YbF_3-undoped glass (x = 0) melted under a reductive atmosphere to confirm the behavior of the host glass, and (3) YbF_3-doped glass (x = 0.2) melted under an oxidizing atmosphere to obtain a reference sample that did not contain Yb^{2+} ions. Thus, a total of nine glass samples were prepared in the first phase of the study.

The concentration of YbF_3 was experimentally determined in advance to avoid concentration quenching. All fluoride raw materials were high purity grade (Fe, Ni, Co, Cu < 50 ppb, O < 100 ppm) and obtained from Central Glass Co., Ltd. After the raw materials were mixed, NH_4FHF (1% by weight) was added to each fluoride mixture, followed by heating at 350°C for 1 h in a glassy carbon crucible to eliminate oxide impurities. These batches were then melted at 1000°C for 1 h. During melting, the atmosphere in the furnace was chosen for different conditions: 5 l/min of 3% H_2 + 97% Ar (H_2/Ar) gas for the reductive atmosphere, and 10 l/min of 0.5% Cl_2 + 99.5% N_2 (Cl_2/N_2) gas for the oxidative atmosphere. After the batches had melted, the crucibles were cooled on a room temperature copper plate without casting the melts. The entire procedure, from mixing the raw materials to cooling the melt, was carried out in an N_2-filled glove box directly equipped with an atmosphere controllable furnace.

The glass transition temperatures (T_g) and crystallization temperatures (T_x) of the glasses were measured using a Rigaku DSC8270 differential scanning calorimeter. The excitation and emission spectra of the obtained glasses were measured at 300 K using a Jasco FP-6500 spectrofluorometer. The transmittance spectra of the glasses were measured using a Hitachi U-4100 spectrophotometer. The X-ray diffraction (XRD) spectra of the glasses were measured

by Rigaku Ultima III X-Ray Diffractometer. Finally, the QEs of the Yb^{2+} fluoride glasses were measured using a FP-6500 spectrofluorometer equipped with a JASCO ILF-533 integrating sphere. Samples (6 × 6 × 1.5 mm) were polished and placed into the integrating sphere. The diameter of the excitation beam on the sample was approximately 5 mm. The internal (η_{in}) and external (η_{ex}) QEs were calculated [19] as,

$$\eta_{in} = \frac{\int \lambda P(\lambda) \mathrm{d}\lambda}{\int \lambda [E(\lambda) - R(\lambda)] \mathrm{d}\lambda} \tag{4-1}$$

and

$$\eta_{ex} = \frac{\int \lambda P(\lambda) \mathrm{d}\lambda}{\int \lambda E(\lambda) \mathrm{d}\lambda}, \tag{4-2}$$

where $E(\lambda)/h\nu$, $R(\lambda)/h\nu$, and $P(\lambda)/h\nu$ correspond to the number of photons during excitation and the reflectance and emission wavelengths of the sample, respectively.

Table 1. Composition of fluoride glasses

	AlF_3	HfF_4	ZrF_4	BaF_2	CaF_2	MgF_2	SrF_2	YF_3	YbF_3	T_g	T_x
Al	35			10	20	10	10	15 − x	x	427	531
Al–Hf	30	10		11	13	24	3	9 − x	x	405	494
Al–Zr	30		10	11	13	24	3	9 − x	x	403	483

Compositions and temperatures are in mole percentages and degrees Celsius.

4.3 Results and discussion

Fig. 1 shows photographs of the glasses (diameter: 35 mm and thickness: 6 mm) melted under an H_2/Ar (reductive) atmosphere excited at different wavelengths. The glasses melted under the Cl_2/N_2 (oxidative) atmosphere did not exhibit any luminescence when excited with UV light (photograph not shown). As can be seen in Figs. 1(b) and (c), YbF_3-doped Al glass excited with near-UV (365 nm) and deep-UV (254 nm) wavelengths exhibited strong white luminescence. The broad emission from the Yb^{2+} centers is due to 4f5d → 4f transitions [7]; therefore, these results indicate that the divalent Yb ions are stabilized in the Al glass. On the other hand, the intensity of white luminescence from the Al–Hf and Al–Zr glasses excited with near-UV light (365 nm) was lower than that of the Al glass, while the Al–Zr and Al–Hf glasses exhibited strong bluish luminescence following deep-UV (254 nm) excitation, suggesting the possible generation of other emission centers in the Zr- and Hf-containing glasses.

Fig. 2 shows the excitation and emission spectra for the Yb^{2+}:fluoride glasses excited with near-UV light (300 nm). The detail of the transitions and energy diagram for Yb^{2+} ions in CaF_2 hosts have been described by Loh [20, 21] and Nicoara et al. [22] as shown in Fig.3. Each 5d level of the $4f^{13}5d(^2F_{5/2})$ and $4f^{13}5d(^2F_{7/2})$ orbitals splits in the crystal field into t_2 and e levels [9]; therefore, at least four strong excitation bands are typically observed. With the Al glass, which is an amorphous host, five excitation peaks were also observed (Fig. 2). The emission spectrum of the Al glass covers the entire visible region, and the full width at half maximum (FWHM) of its white luminescence was 202 nm. The white emission intensity notably decreased with the addition of Hf and Zr. Note that because the excitation spectrum of the Al–Zr glass increased below 275 nm, the fluorescence properties of this material excited at short wavelengths were investigated and are presented below.

The excitation and emission spectra of the doped and undoped Al–Hf and Al–Zr glasses excited with deep-UV light (235 nm), which led to blue emissions, are presented in Fig. 4. Strong bluish-white light emissions centered around 450 nm were observed, even for the YbF_3-undoped glasses. In addition, the emission intensities decreased with the incorporation of YbF_3. Here, these bluish broadband emissions are attributed to the reduced species, Zr^{4+} and Hf^{4+}. Fluorohafnate glasses melted under a 5% H_2/Ar atmosphere were previously found to exhibit luminescence around 340–460 nm under X-ray excitation, and the presence of Hf^{3+} in these glasses was also suggested [23]. In addition, the results of an electrochemical study of a Yb-doped fluorozirconate melt suggested the presence of both Yb^{2+} and Zr^{3+} [24]. It is believed, on the basis of these reports that Zr^{3+} and Hf^{3+} exist in the Al–Zr and Al–Hf glasses melted under an H_2/Ar atmosphere.

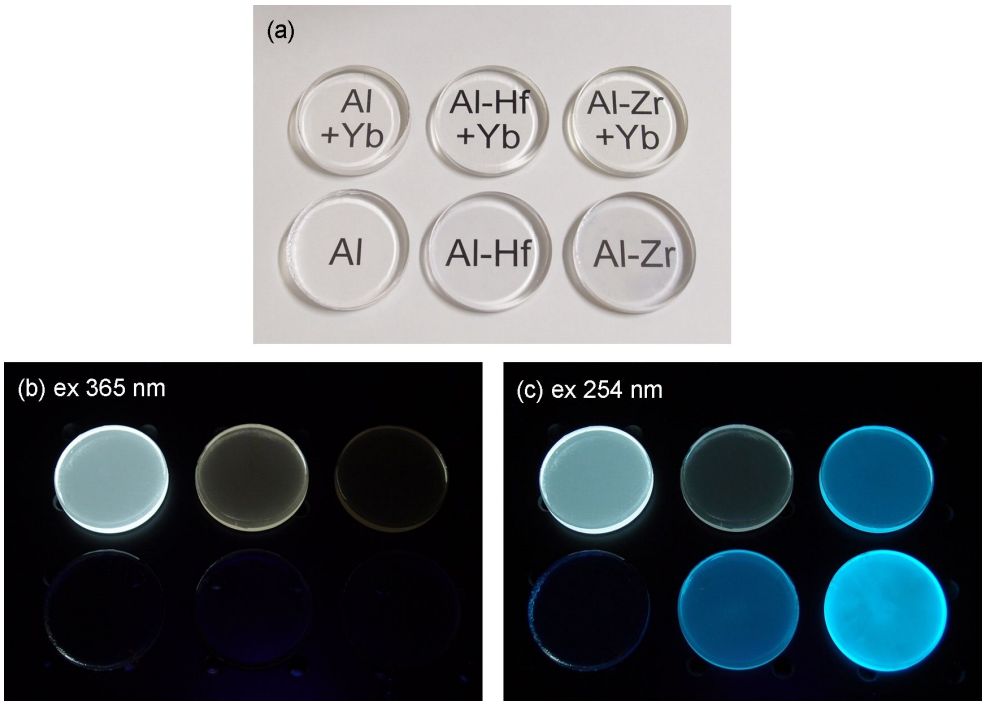

Fig. 1. Yb^{2+}-containing glasses melted under H_2/Ar atmosphere. (a) Illuminated by fluorescent light, (b) excited at 365 nm, and (c) excited at 254 nm. Top three glasses in each photograph were doped with YbF_3, and bottom three glasses were not.

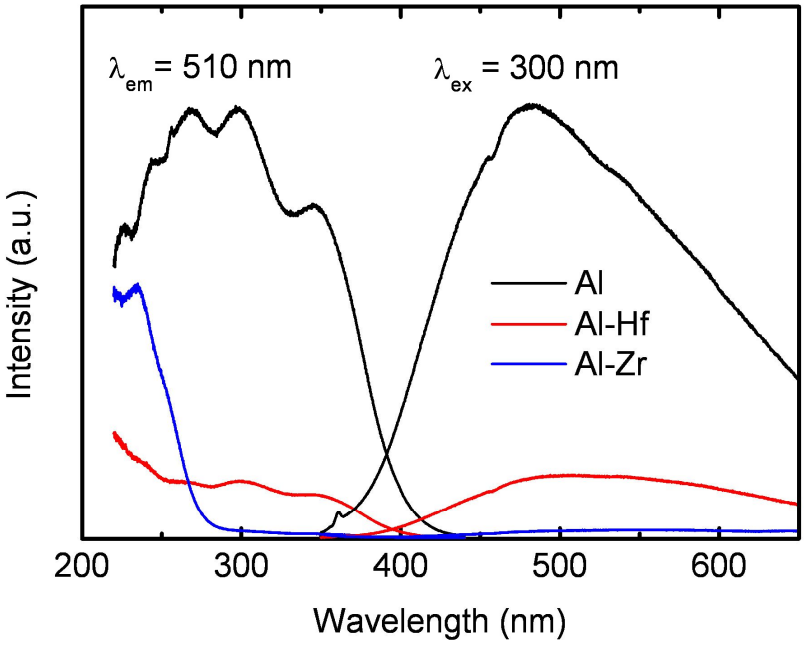

Fig. 2. Excitation and emission spectra of Yb^{2+}:fluoride glasses melted under an H_2/Ar atmosphere.

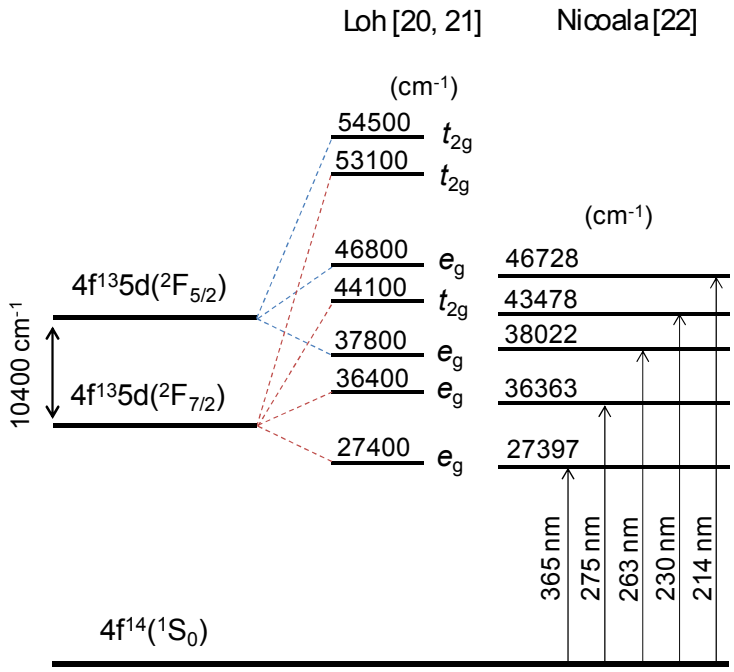

Fig.3. Energy level diagram for Yb^{2+} ions in CaF_2 host.

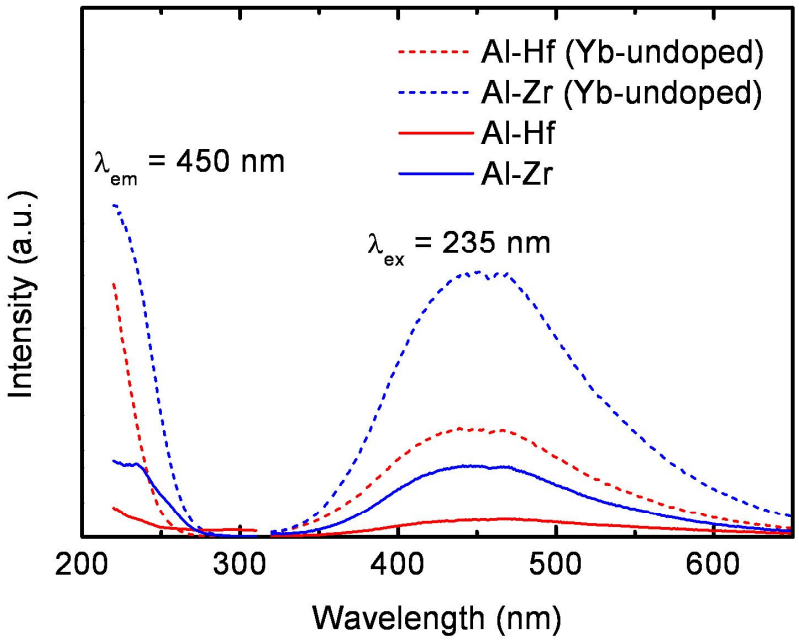

Fig. 4. Excitation and emission spectra of Al–Hf and Al–Zr glasses with and without Yb. These glasses were melted under an H_2/Ar atmosphere.

4.4. Estimates of reduction ratios for Yb^{3+} in Al, Al–Hf, and Al–Zr glasses

Because white luminescence in these glasses was considered to originate from Yb^{2+}, the reduction ratio, $\Delta = Yb^{2+}/(Yb^{2+} + Yb^{3+})$, was estimated by decreasing the absorbance of trivalent Yb^{3+} ($^2F_{7/2} \rightarrow {}^2F_{5/2}$) around 972 nm and comparing the transmittance spectra of glasses melted under Cl_2/N_2 and H_2/Ar atmospheres.

Fig. 5 shows the transmission spectra of 6.0-mm-thick fluoride glasses melted under different atmospheres. It can be seen from Fig. 5(a) that a new absorption band below 400 nm appeared in the spectra of the three YbF_3-doped glasses following melting under an H_2/Ar atmosphere, while absorption edges appeared below 200 nm in the spectra of the three glasses melted under a Cl_2/N_2 atmosphere. These results suggest that the reduction of Yb^{3+} not only occurred in the Al glass, but also in the Al–Hf and Al–Zr glasses. Although the previously reported SYAM glass was grayish in color due to the reductive atmosphere [18], the transmittance of the Al glass in the visible region (>425 nm) was independent of the melting atmosphere. On the other hand, the transmittance of the Al–Hf and Al–Zr glasses slightly decreased when melted under H_2/Ar. Therefore, the Al glass provided the best composition to maintain transmittance, even under reductive conditions.

The transmittance of the undoped fluoride glasses melted under an H_2/Ar atmosphere can be seen in Fig. 5(b). The absorption edges in the spectra of the host glasses are less intense than those of the Yb-doped glasses, and the increased intensity of the absorption in the UV region in Fig. 5(a) indicates the generation of Yb^{2+}. In addition, only the Al–Zr glass that melted under an H_2/Ar atmosphere exhibited wavelength-independent absorption. This type of absorption is generally considered to occur because of aggregates of carbon black, metal, or lower valence cations such as Zr^{3+} [25]. Aggregates of Zr^{3+} in the Al–Zr glass may be the main source of absorption because the Al and Al–Hf glasses did not exhibit any wavelength-independent

losses. Notably, this wavelength-independent loss in the Al–Zr glass could be almost completely suppressed by incorporating 0.2 mol% YbF_3.

Fig. 6 shows the normalized transmittance at 972 nm, which corresponds to the Yb^{3+} ($^2F_{7/2}$ → $^2F_{5/2}$) transition, from which the background losses described in Fig. 5(a) have been deducted. The reduction ratio Δ was estimated from the decrease in absorbance for the glasses melted under different atmospheres, as shown in the inset of Fig. 6. As a result, the Δ values were calculated to be 11 ± 1% for the Al glass, 9 ± 1% for the Al–Hf glass, and 10 ± 1% for the Al–Zr glass, considering the accuracy of the measured quantities of raw materials used. These results revealed that the percentage of Yb^{2+} ions in the different glasses was nearly the same. However, the intensity of the white luminescence of the Al–Hf and Al–Zr glasses was much lower than that of the Al glass, suggesting that energy transfer occurs between the Yb^{2+} and Hf^{3+}/Zr^{3+} ions; thus, the co-existence of these reduced species quenches not only the white luminescence from Yb^{2+}, but also the bluish luminescence from Hf^{3+}/Zr^{3+}.

Fluoride glasses are typically highly doped with ZrF_4 or HfF_4, particularly those used in optical fiber applications, to lower Tg (<300°C) and reproducibly obtain optical fibers. It is difficult in these glass systems to obtain efficient white luminescence of Yb^{2+} due to the presence of Hf^{3+}/Zr^{3+}. T_g and T_x of the Al, Al–Hf, and Al–Zr glasses produced in this study are listed in Table 1. As can be seen in the table, the elimination of Hf/Zr from the fluoride glass compositions resulted in high T_g and T_x values.

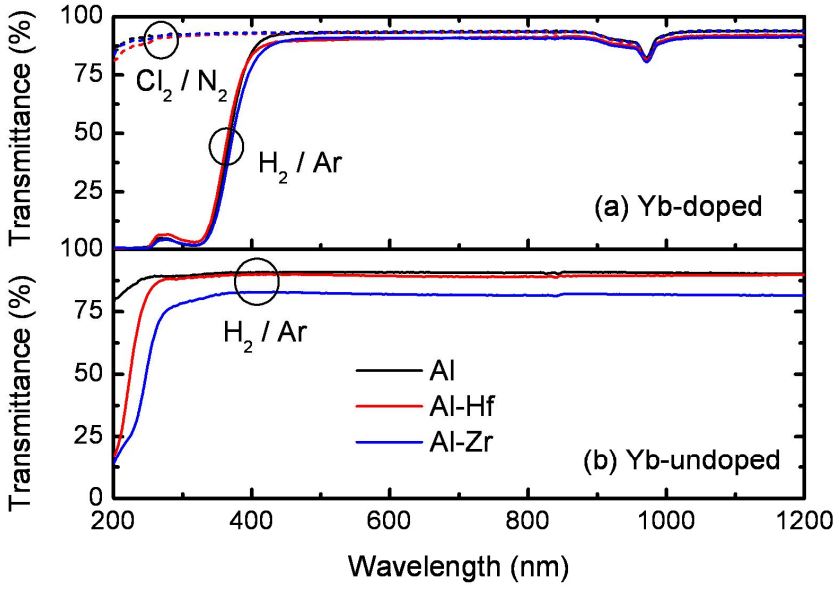

Fig. 5. Differences in transmittance of fluoride glasses melted under different atmospheres.

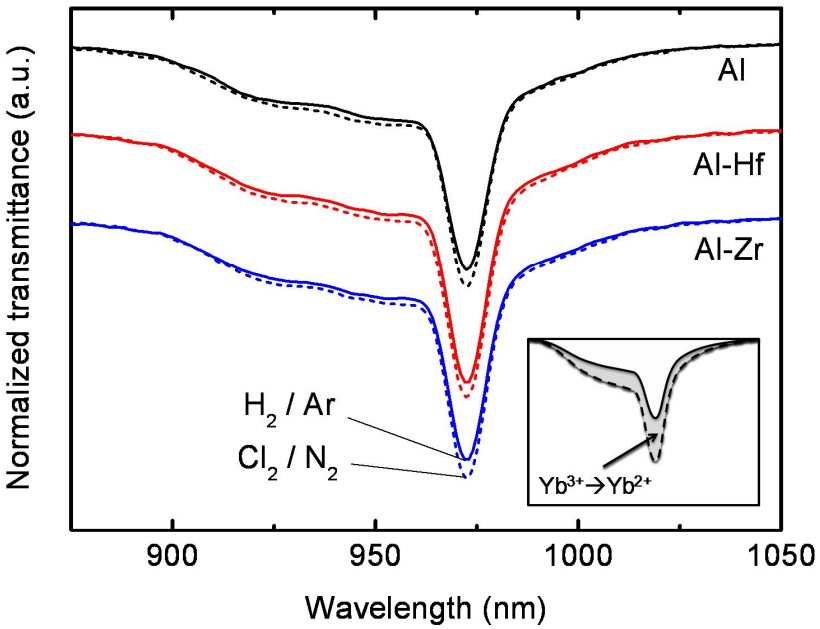

Fig. 6. Differences in transmittance of fluoride glasses caused by a reductive atmosphere at wavelength of Yb^{3+} ($^2F_{7/2} \rightarrow {}^2F_{5/2}$) transition.

4.5 Enhancement of white luminescence of Al glass

As discussed above, the Al glass exhibited the highest white luminescence intensity of the prepared glass samples. Host glasses, such as those with fluoride, chloride, bromide, or iodide compositions, which generally have low phonon energies, have higher emission efficiencies due to the low non-radiative decay rates and high radiative emission rates of rare-earth ion levels [26, 27]. Thus, we primarily investigated the incorporation of non-fluoride halide ions (Cl^-) into Al glass to intensify their white luminescence. The glass compositions used in this second phase of the study are listed in Table 2. The raw material, BaF_2, was replaced with $BaCl_2$ and $SrCl_2$. The concentration of YbF_3 (x = 0.2) and the reduction conditions were the same as those used to prepare the initial Yb-doped Al glass. Note that the "Al glass" in the first entry of Table 2 has exactly the same composition as that in Table1.

The excitation and emission spectra of Yb^{2+}:Al glasses containing added chloride can be seen in Fig. 7. An excitation peak near 365 nm can be observed in each spectrum. Notably, as more fluoride ions are replaced with chloride ions (BaF_2 → $BaCl_2$; Al → Al-1 → Al-2), the intensity of the 365 nm peak is increased remarkably. This wavelength is close to the bandgap of GaN (3.4 eV); therefore, Yb^{2+}:fluoride glasses can be excited by conventional GaN semiconductor light sources. In addition, when $BaCl_2$ was substituted with the same amount of $SrCl_2$ (Al-2 → Al-3), the excitation peak shifted to a longer wavelength. The chromaticity diagram corresponding to the emission spectra are shown later (Fig.11 in section 4.7). The luminescence color of Al-2 shifted to blue, while that of Al-3 returned to white because the emission intensity of Al-3 in the green and red regions was improved remarkably.

In order to investigated the structures in those bulks, the XRD spectra of Yb^{2+}: Al glasses demonstrated in this section are shown Fig. 8. The XRD spectra of Al , Al-1, Al-3 glasses do not show any crystalline peak, however, only that of Al-2 exhibits crystalline peak

corresponding to the $BaCl_2$ crystalline, while the glass is also transparent. This result means that composition of Ba in the Al-2 glass is too rich then the composition moved to out of glass-form region. As can be seen in Fig. 7, the bandwidth of the excitation and emission spectra of Al-2 glass is narrower than others because of crystallization.

The incorporation of non-fluoride halide ions in AlF_3-based fluoride glasses has been discussed [28], and promotion of the reduction of rare earth ions has been confirmed experimentally. The reduction ratio Δ of the Al-3 glass was estimated to be 45% using the same procedure as that in Fig. 6. Because this value is approximately four times greater than that of the original Al glass, it can be concluded that the number of Yb^{2+} ions increased in the fluoride glass.

Xia et al. recently prepared Yb^{2+}-containing silica glass (SiO_2–Al_2O_3–Yb_2O_3) by heating the relevant mixture at 1950°C for 8 h under vacuum conditions [29]. The excitation band of this glass was wider (up to 500 nm) than that of Al-3 glass; therefore, reabsorbance of the blue light emitted from Yb^{2+} may have led to a decrease in the luminescence efficacy. On the other hand, because the excitation band of the Al-3 glass was below 400 nm, the overlap of the excitation and visible emission bands was minimized in this glass.

Table 2. Composition of Al glasses with added chloride

	AlF_3	BaF_2	$BaCl_2$	SrF_2	$SrCl_2$	CaF_2	MgF_2	YF_3	YbF_3
Al	35	10		10		20	10	15 − x	x
Al-1	35	5	5	10		20	10	15 − x	x
Al-2	35		10	10		20	10	15 − x	x
Al-3	35			10	10	20	10	15 − x	x

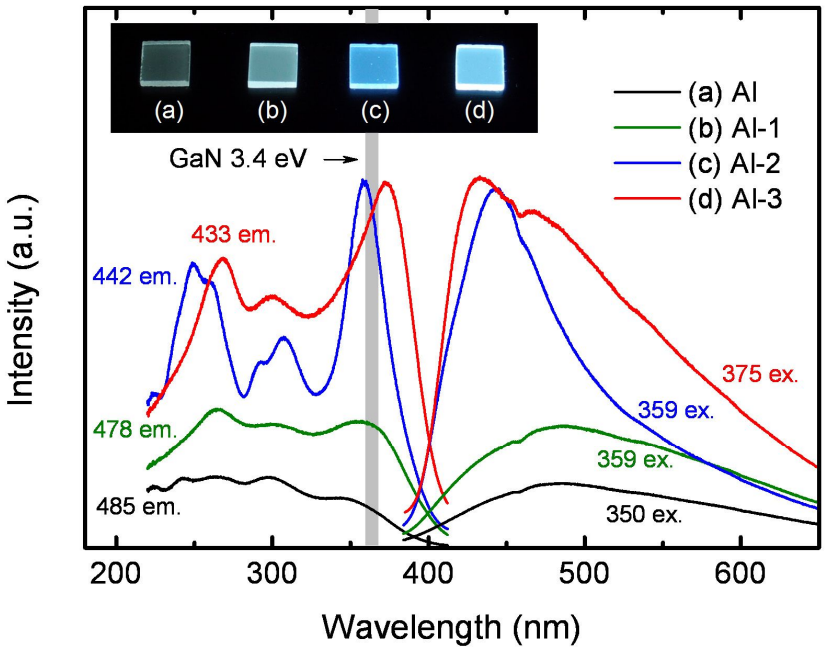

Fig. 7. Excitation and emission spectra for Yb^{2+}:Al glasses with added chloride ions. Inset photographs are of samples excited at 365 nm.

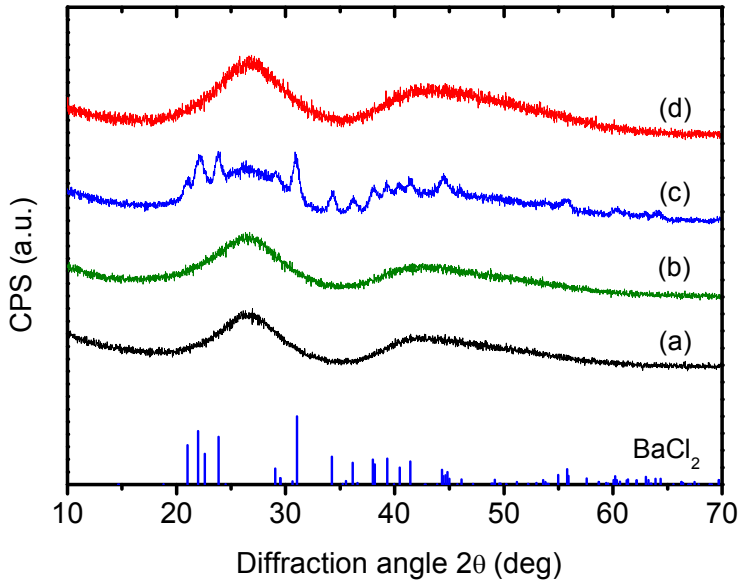

Fig.8. XRD spectra of Yb^{2+}:Al glasses melted under a reductive atomosphere.

4.6 Quantum efficiencies of Yb^{2+}:Al glasses

Finally, the QEs of the Al glasses were measured and are listed in Table 3. The highest QE was obtained for the Al-3 glass, with η_{in} calculated to be 42% and η_{ex} calculated to be 34%. On the other hand, the QE of Yb^{2+}:β-SiAlON (a green phosphor) measured at an excitation wavelength of 480 nm was reported to be $\eta_{in} = 28\%$ and $\eta_{ex} = 9\%$ using the same approach [10]. Thus, the Yb^{2+}-doped fluoride glass had moderately higher QE than the Yb^{2+}-doped crystalline phosphor. Because these Yb^{2+} fluoride glasses demonstrated efficient visible emission under near-UV excitation, further improvements to the reduction ratio and optimization of the glass composition should enable the development of even more efficient white emission glasses.

Table 3. Quantum efficiencies of Al glasses excited with near-UV light

	Excitation wavelength (nm)	η_{in}	η_{ex}
Al	350	10	5
Al-1	359	22	15
Al-2	359	34	23
Al-3	375	42	34

4.7 Improvement of color rendering of Yb^{2+}:AlF_3-based glass using melting process

As a result of chloride incorporation to Yb^{2+}:fluoride glasses, the intensity of white emission was increased dramatically. However, the emission color of the glass is a little bluish. In order to improve the color rendering, the red spectrum was preferred to be enhanced. In the case of current conventional LED illuminations fabricated by the combination of blue GaN-LD and yellow YAG:Ce^{3+} phosphor, the lack of the red spectrum is compensated by mixing the red phosphor such as $CaAlSiN_3$:Eu^{2+} [30], SiAlON:Eu^{2+} [31]. However, these phosphors can not be mixed with fluoride melts at the same time, because these phosphors would be damaged in the fluoride melts at high temperature.

In this section, we focused on Mn^{2+}, which emits orange–red light, as the candidate of the dopant to Yb^{2+}:fluoride glass. The optical transition of Mn^{2+} in ZBLA (ZrF_4–BaF_2–LaF_3– AlF_3) and HBL (HfF_4–BaF_2–LaF_3) glasses melted under Ar atmosphere were investigated [32, 33]. Mn^{2+} doped fluoride glass exhibits orange emission at 17400 cm^{-1} (575 nm), however, Mn^{2+} doped AlF_3 based glass melted under a reductive atmosphere have not been reported yet.

In order to improve the color rendering of Al-3 glass, two compositions were experimented by replacing MgF_2 of Al-3 glass to MnF_2: Al-3-Mn1 glass (MgF_2 → MnF_2:0.05 mol%) and Al-3-Mn2 glass (MgF_2 → MnF_2:0.3 mol%). Each mixture was melted under an H_2/Ar atmosphere as same as Al-3 glass. As a result, the Al-3-Mn1 glass was transparent while the Al-3-Mn2 glass was translucent. The excitation and emission spectra of MnF_2 doped Yb^{2+}:fluoride glass were shown in Fig.9. By incorporating 0.05 mol% of MnF_2, the emission intensity around 640 nm increased remarkably while the emission intensity 400–580 nm was suppressed. Notably, the FWHM of Al-3-Mn1 was 301 nm and it covers whole of the visible

wavelength range. Furthermore, the more MnF_2 was added to the glass (Al-3-Mn1 → Al-3-Mn2), the new emission peak was observed at 406 nm. Here, we measured the XRD spectrum of Mn doped glasses as shown in Fig.10. Al-3 and Al-3-Mn1 glass do not show any crystalline peak but Al-3-Mn2 shows weak crystalline peak corresponding to $SrCl_2$. The luminescence properties of Yb^{2+} doped alkaline earth fluorohalides MFX (M = Ca, Sr, Ba; X = Cl, Br) were investigated by W. J. Schipper et. al [34], and Yb^{2+} doped $Sr_{0.99}Yb_{0.01}FCl$ crystalline exhibits narrow emission band around 400 nm. Referring to the report, the emission peak at 406 nm of Al-3-Mn2 glass may have originated from SrYbFCl type crystalline deposited in the glass.

As discussed above, by incorporating MnF_2 slightly to Yb^{2+}:fluoride glasses, the emission color transformation from bluish to white is possible. The chromaticity diagram of white emission glasses demonstrated in this section is summarized in Fig.11. The color coordination of Al-3-Mn1 glass, which emits whiter light, was (X, Y) = (0.325, 0.307).

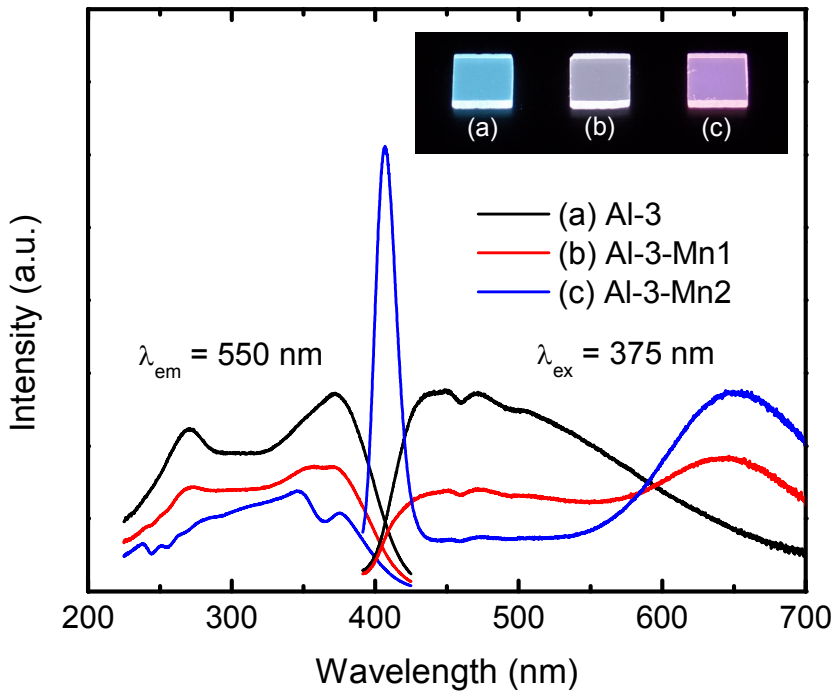

Fig. 9. Excitation and emission spectra of MnF_2 doped Al-3 glasses.

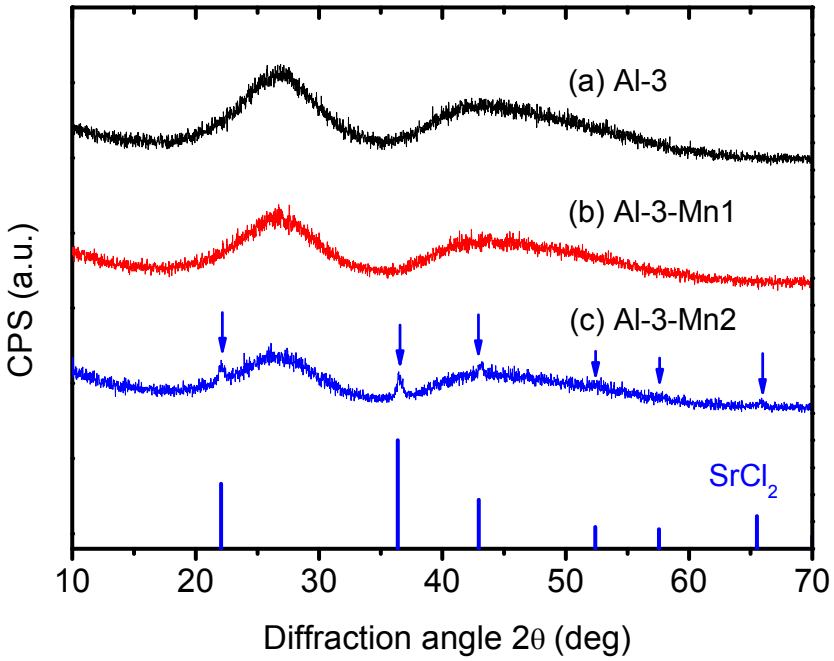

Fig.10. XRD spectra of Mn^{2+}-Yb^{2+}:Al glasses melted under a reductive atmosphere.

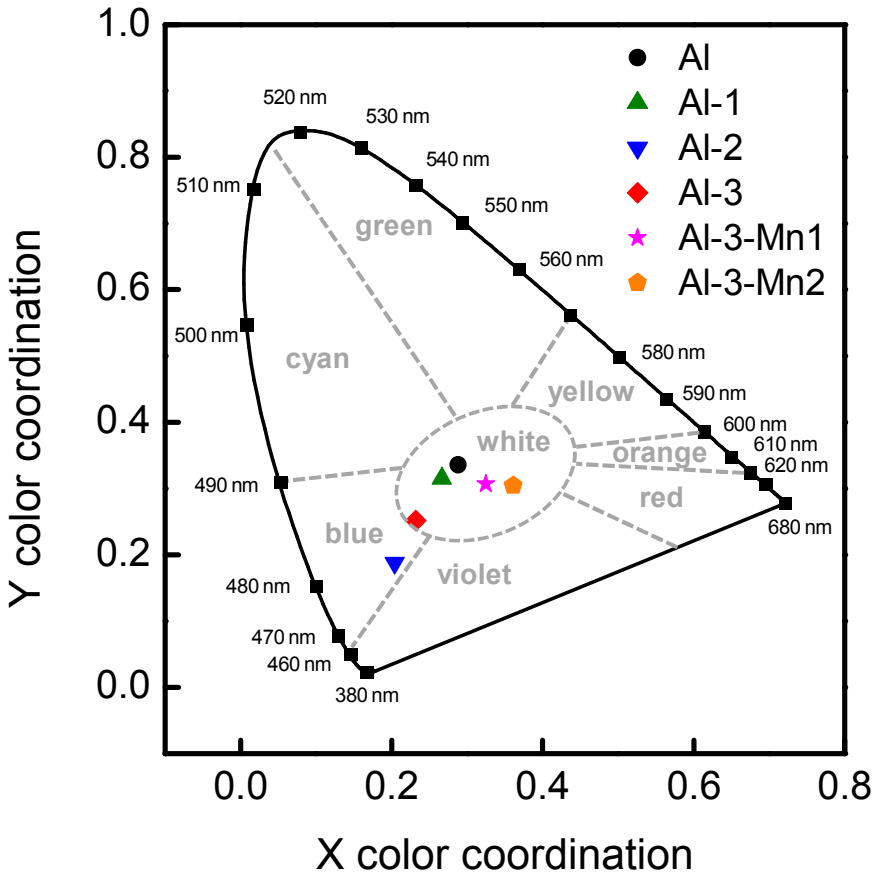

Fig.11. Chromaticity diagram of Yb^{2+} fluoride glasses.

4.8 Conclusion

We successfully prepared white luminescent Yb^{2+}:AlF_3-based fluoride glasses that were efficiently excited with near-UV light. Fluoride glasses containing Hf or Zr that melted under an H_2/Ar atmosphere exhibited bluish white luminescence, but the co-existence of Yb^{2+} and Hf^{3+}/Zr^{3+} resulted in the suppression of white luminescence. On the other hand, the white luminescence of Yb^{2+} was notably intensified by incorporating chloride through replacing BaF_2 with $BaCl_2$ and $SrCl_2$. Although the highest reduction ratio ($\Delta = Yb^{2+}/(Yb^{2+} + Yb^{3+})$) was only 45% for the chloride-containing glass, η_{in} was 42% and η_{ex} was 34%. By incorporating chlorides to Yb^{2+}:glass, the emission color was turned to be bluish, however, additional incorporation of MnF_2 can compensate the emission color successfully. Further improvements in the QE are required for practical visible applications; however, such enhancements can be achieved by analyzing the mechanism responsible for chloride incorporation.

Fluoride glass is a low melting, inorganic glass, and it can thus be used as an inorganic material to seal LEDs and optical fibers. In addition, although AlF_3-based glass has a higher T_g than fluorozirconate glass, fiber drawing techniques for AlF_3-based glass have been improved [30]. Therefore, fiber light sources using divalent rare earth ion-doped fluoride glasses will also be possible in the near future.

References

1. K. Bando, K. Sakano, Y. Noguchi, and Y. Shimizu, Journal of Light and Visual Environment **22**, 2 (1998).
2. T. Kasahara, D. Aizawa, T. Irikura, T. Moriyama, M. Toda, and M. Iwamoto, Journal of Light and Visual Environment **30**(2), 95 (2006).
3. T. Fukui, K. Kamon, J. Takeshita, H. Hayashi, T. Miyachi, Y. Uchida, S. Kurai, and T.Taguchi, Japanese Journal of Applied Physics, **48**, 112101 (2009).
4. T. Taguchi, Journal of Light and Visual Environment **30**, 177 (2006).
5. H. Daicho, T. Iwasaki, K .Enomoto, Y. Sasaki, Y. Maeno, Y. Shinomiya, S. Aoyagi, E. Nishibori, M. Sakata, H. Sawa, S. Matsuishi, and H. Hosono, Nature Communications **3**, 1132 (2012).
6. N. Guo, H. You, Y. Song, M. Yang, K. Liu, Y. Zheng, Y. Huang, and H. Zhang, Journal of Materials Chemistry **20**, 9061 (2010).
7. G. G. Li, D. L. Geng, M. M. Shang, C. Peng, Z. Y. Cheng, and J. Lin, Journal of Materials Chemistry **21**, 13334 (2011).
8. Y. Song, G. Jia, M. Yang, Y. Huang, H. You, and H. Zhang, Applied Physics Letters 94(9), 091902 (2009).
9. R. J. Xie, N. Hirosaki, M. Mitomo, K. Uheda, T. Suehiro, X. Xu, Y. Yamamoto, and T. Sekiguchi, The Journal of Physical Chemistry B, 109, 9490 (2005).
10. L. Liu, R. J. Xie, N. Hirosaki, T. Takeda, C. N. Zhang, J. Li, and X. Sun, Science and Technology of Advanced Materials, **12**, 034404 (2011).
11. H. Guo, X. Wang, J. Chen, and F. Li, Optics Express **18**(18), 18900 (2010).
12. H. Guo, R. Wei, and X. Liu, Optics Letters **37**(10), 1670 (2012).

13. R. F. Wei, C. G. Ma, Y. Wei, J. Y. Gao, and H. Guo, Optics Express **20**, 29743 (2012).

14. H. Yang, G. Lakshminarayana, Y. Teng, S. Zhou, and J. Qiu, Journal of Materials Research **24**(5), 1730 (2009).

15. X. L. Liang, Y. X. Yang, C. F. Zhu, S. L. Yuan, G. R. Chen, A. Pring, and F. Xia, Applied Physics Letters **91**, 091104 (2007).

16. H. Masai, T. Fujiwara, S. Matsumoto, Y. Takahashi, K. Iwasaki, Y. Tokuda, and T. Yoko, Optics Letters **36**, 2868 (2011).

17. D. Chen, Y. Yu, H. Lin, P. Huang, F. Weng, Z. Shan, and Y. Wang, Optics Letters **34**(19), 2882 (2009).

18. J. W. M. Verwey and G. Blasse, Journal of Physics and Chemistry of Solids **53**, 1152 (1992).

19. K. Ohkubo and T. Shigeta, The Illuminating Engineering Institute of Japan **83**, 87 (1999).

20. E. Loh, Physical Review **175**, 533 (1968)

21. E. Loh, Physical Review **184**, 348 (1969)

22. I. Nicoara, L. Lighezan, M. Enculescu, and I. Enculescu, Journal of Crystal Growth **310**, 2026 (2008).

23. I. Kamenskikh, V. Mikhailin, D. Spassky, S. Batygov, L. Dmitruk, L. Moiseeva, N. Vinogradova, M. Kirm, and G. Zimmerer, Nuclear Instruments and Methods in Physics Research Section A **486**, 288(2002).

24. D. R. MacFarlane, J. Javorniczky, P. J. Newman, Journal of Non-Crystalline Solids **256&257**, 36 (1999).

25. M. Poulain and G. Maze, Chemtronics **3**,77 (1988).

26. Y. Hatefi, N. Shahtahmasebi, A. Moghimi, and E. Attaran, Journal of Rare Earths **29**(5), 484 (2011).

27. K. Annapurna, R. N. Dwivedi, and S. Buddhudu, Materials Letters **53**, 359 (2002).

28. T. Yano, K. Yamazaki, S. Shibata, M. Yamane, and S. Inoue, Journal of the Ceramic Society of Japan **105**(8), 635 (1997).

29. C. Xia, G. Xhou, Y. Han, X. Zhao, and L. Hou, Optical Materials **34**, 769 (2012).

30. X. Piao, K. Machida, T. Horikawa, H. Hanzawa, Y. Shimomura, and N. Kijima, Chemistry of Materials **19**(18), 4592 (2007).

31. H. Naoto, R.J. Xie, K. kimoto, T. Sekiguchi, Y Yamamoto, T. Suehiro, and M. Mitomo , Applied Physics Letters 86(21) 211905 (2005).

32. L. N. Feuerhelm, S. M. Sibley, and W. A. Sibley, Journal of Solid State Chemistry **54**, 164 (1984)

33. M. G. Drexhage, C. T. Moynihan, and M. Saleh, Materials Research Bulletin **15**, 213 (1980).

34. W. J. Schippere, and G. Blasse, Journal of Solid State Chemistry **94**, 418 (1991)

35. J. Nakanishi, Y. Horiuchi, T. Yamada, O. Ishii, M. Yamazaki, M. Yoshida, and Y. Fujimoto, Optics Letters **36**, 1836 (2011).

List of Publications

Chapter 1

"Preparation of ZBLAN fibres and analysis of its defects,"

Hideyuki Okamoto, Ken Kasuga, Natsuya Nishimura, Yoshinori Kubota, Masaaki Sakakura, Yasuhiko Shimotsuma, and Kiyotaka Miura,

Electronics Letters, to be submitted.

Chapter 2

"Over-10 mW broadband Pr^{3+}:ZBLAN-fibre light source at 635 nm pumped by GaN LD,"

Hideyuki Okamoto, Ken Kasuga, Ikunari Hara, and Yoshinori Kubota,

Electronics Letters, Vol. 44, pp.1346~1347 (2008)

"Visible–NIR tunable Pr^{3+}-doped fiber laser pumped by a GaN laser diode,"

Hideyuki Okamoto, Ken Kasuga, Ikunari Hara, and Yoshinori Kubota,

Optics Express, Vol. 17, pp. 20227~20232 (2009)

"Ultra-Wideband Tunable RGB Fiber Laser,"

Hideyuki Okamoto, Ken Kasuga, Ikunari Hara, and Yoshinori Kubota,

in Conference on Lasers and Electro-Optics/International Quantum Electronics Conference, OSA Technical Digest (CD) (Optical Society of America, 2009), paper CFB7.

"Expanded color gamut reproduced by multi-color fluoride fibre lasers,"

Hideyuki Okamoto, Ken Kasuga, Yoshinori Kubota, Masaaki Sakakura, Yasuhiko

Shimotsuma, and Kiyotaka Miura,

Electronics Letters, to be submitted.

Chapter 3

"Efficient 521 nm all-fiber laser: splicing Pr^{3+}-doped ZBLAN fiber to end-coated silica fiber,"

Hideyuki Okamoto, Ken Kasuga, and Yoshinori Kubota,

Optics Letters, Vol. 36, pp.1470~1472 (2011)

"All-fiber laser resonator: Splicing fluoride fiber to dielectric-mirror-coated silica fiber,"

Hideyuki Okamoto, Ken Kasuga, and Yoshinori Kubota,

Optics Express, to be submitted.

Chapter 4

"White emission of Yb^{2+}:fluoride glasses efficiently excited with near-UV light,"

Hideyuki Okamoto, Ken Kasuga, Yoshinori Kubota, Natsuya Nishimura, Hiromi Kawamoto, Koichi Miyauchi, Yasuhiko Shimotsuma, and Kiyotaka Miura,

Optics Express, Vol. 21, pp. 22043~22052 (2013)

"Mn^{2+}-Yb^{2+} codoped fluoride glass phosphors for high color rendering light emitting diodes,"

Hideyuki Okamoto, Ken Kasuga, Yoshinori Kubota, Masaaki Sakakura, Yasuhiko Shimotsuma, and Kiyotaka Miura,

Applied Physics Letters, to be submitted.

Acknowledgements

The present thesis has been carried out at the Graduate School of Engineering in Kyoto University under the direction of Professor Kiyotaka Miura.

First of all, the author wishes to express special thanks to Professor Kiyotaka Miura, who supervised the present work, for his encouragement, and for moral support. The careful readings of this thesis by Professor Kazuyuki Hirao and Professor Katsuhisa Tanaka are gratefully acknowledged. The author profoundly grateful to Associate Professor Yasuhiko Shimotsuma and Associate Professor Masaaki Sakakura for giving technical help and encouragement.

The author would like to thank the students of Miura laboratory giving encouragement and support all throughout the research study.

The author would like to express his thanks to the members of Central Glass Co., Ltd, in the following. The author is deeply grateful specially to Mr. Yoshinori Kubota for his sincere encouragement and continuing supports on the whole part of this thesis. Mr. Natsuya Nishimura and Mr. Ken Kasuga have been giving enormous help and support for preparing fluoride glasses and drawing fluoride fibers. The high purity fluoride raw materials used in this thesis were synthesized by Mr. Hiromi Kawamoto. The author also thanks to Mr. Ikunari Hara, Mr. Hitoshi Omuro and Mr. Takuya Teshima for their experimental support concerning splicing fluoride fibers.

Finally, the author would like to express his thanks to his wife Mrs. Ryoko Okamoto, and their daughters Yuki, Kasumi and Mitsuki Okamoto for their understanding, supports, and hearty encouragements.

Hideyuki Okamoto

Copyrights and Sources